Designing metamaterials with programmable nonlinear responses and geometric constraints in graph space

Marco Maurizi[1]*†, Derek Xu[2]†, Yu-Tong Wang[3]†, Desheng Yao[1], David Hahn[1], Mourad Oudich[3,4], Anish Satpati[1], Mathieu Bauchy[5], Wei Wang[2], Yizhou Sun[2], Yun Jing[3], Xiaoyu Rayne Zheng[1]*

[1]Department of Materials Science and Engineering, University of California Berkeley; Berkeley, 94720, USA.

[2]Department of Computer Science, University of California Los Angeles; Los Angeles, 90095, USA.

[3]Graduate Program in Acoustics, Penn State University; Pennsylvania 16802, USA.

[4]Universite' de Lorraine, CNRS, Institut Jean Lamour; F-54000 Nancy, France.

[5]Department of Civil and Environmental Engineering, University of California Los Angeles; Los Angeles, 90095, USA.

*Corresponding authors. Emails: marcomaurizi@berkeley.edu, rayne23@berkeley.edu

†These authors contributed equally to this work.

Abstract:

Advances in data-driven design and additive manufacturing have significantly accelerated the development of truss metamaterials – three-dimensional truss networks – offering exceptional mechanical properties at a fraction of the weight of conventional solids. While existing design approaches can generate metamaterials with target linear properties, such as elasticity, they struggle to capture complex nonlinear behaviors and to incorporate geometric and manufacturing constraints – including defects – crucial for engineering applications. Here, we present GraphMetaMat, an autoregressive graph-based framework capable of designing three-dimensional truss metamaterials with programmable nonlinear responses, originating from hard-to-capture physics such as buckling, frictional contact and wave propagation, along with arbitrary geometric constraints and defect tolerance. Integrating graph neural networks, physics biases, imitation learning, reinforcement learning, and tree search, we show that GraphMetaMat can target stress-strain curves across four orders of magnitude and vibration transmission responses with varying attenuation gaps, unattainable by previous methods. We further demonstrate the use of GraphMetaMat for the inverse design of novel material topologies with tailorable high energy absorption and vibration-damping that outperform existing polymeric foams and phononic crystals, potentially suitable for protective equipment and electric vehicles. This work sets the stage for the automatic design of manufacturable, defect-tolerant materials with on-demand functionalities.

Main Text:

Enabled by additive manufacturing, the architecture of metamaterials can be manipulated to achieve properties and functionalities beyond those of traditional engineering materials at a fraction of their weight[1–6]. Truss metamaterials – a class of low-density metamaterials – are composed of three-dimensional (3D) truss networks[7]. These new classes of materials proved to offer an extremely vast design and property space with unprecedented functionalities, from high stiffness-/strength-to-weight ratio[8,9] and tunable negative Poisson's ratio[10] to programmable elastic[11], piezoelectric anisotropy[1,12] and adaptive assembly and reconfigurability[13–15]. Large-deformation stress-strain and wave transmission responses are nonlinear material fingerprints, representing a material's behaviors to various stimuli, such as energy absorption and dissipation upon impact[16], large deformation upon activation[17], and vibration-borne noise modulation at different frequencies[18]. In truss materials, these nonlinear responses emerge from complex physics such as mechanical instabilities, frictional self-contact, and wave propagation. While exploring these broad design and property spaces is relatively simple using modern computational tools such as finite element (FE) method, automatically identifying a truss network's design for a given property or behavior – the so-called inverse design – remains challenging.

In the quest for inverse designing metamaterials, deep learning-driven approaches have demonstrated significant potential to efficiently optimize or inverse design specific, often linear, properties[10,19–32]. Meanwhile, deep learning methods for the inverse design of molecules[33–36] and crystals[37], bearing similarities with metamaterial design, have shown exceptional results. However, despite their growing popularity in the design of truss structures[38–40] and metamaterials[10,19,29,41], existing methods face critical challenges: they rely on costly data collection, struggle with complex 3D architectures and nonlinear behaviors, lack generalizability, and fail to enforce essential geometric and manufacturing constraints[42,43] – including robustness to fabrication defects – all critical for practical engineering applications. Generative models based on pixel, voxel, point cloud, and mesh representations – including generative adversarial networks[24,44,45] (GANs), variational autoencoders[46] (VAEs), and denoising diffusion models[28,47] – produce diverse metamaterial morphologies but are fundamentally limited by the high resolutions needed to accurately represent slender beams in 3D truss structures[47] and by their extensive labeled-data requirements. Capturing nonlinear phenomena such as frictional self-contact, mechanical instabilities, and wave propagation further exacerbates data demands, exemplified by the ~50,000 high-fidelity labeled samples required to train diffusion models for simpler 2D pixel-based structures[28]. Similarly, conventional graph-based GANs[48] and VAEs[49], and state-of-the-art graph diffusion models for molecular[35,36] and crystal[37] design typically rely on datasets exceeding 100k samples. In molecular systems, atomic connectivity is often implicitly defined by valence rules, allowing inference of chemical bonds from pairwise atomic distances – assumptions that fail in metamaterials, where topology (graph connectivity), geometry (node positions and strut dimensions), and nonlinear performance are tightly coupled and must be jointly optimized. As a result, existing graph-based diffusion models and reinforcement learning (RL) methods developed for molecular[33–36] or truss layout design[38–40] – often optimizing simpler properties such as structural weight under linear conditions without surrogate forward models – are not directly transferable to metamaterial inverse design. Metamaterial-specific methods based on simple vector parameterizations, such as multilayer perceptron (MLP)-based tandem networks[50], offer data efficiency but suffer from limited expressive power and generalizability, restricting them to modifications of existing designs and resulting in limited response variability. Conversely, MLP-based VAEs[51] parametrize truss materials as fixed-size graphs, thus expanding the design space. However, their lack of permutation invariance – essential for graph-structured data – and

generative nature render them highly data-intensive, requiring hundreds of thousands of labeled samples, particularly for nonlinear behaviors.

The practical application of inverse-designed metamaterials is fundamentally constrained by manufacturing limitations, which impose strict geometric requirements and introduce inevitable defects. Structural imperfections – such as delamination, non-uniformities, or missing struts – can cause significant deviations from predicted behavior, yet current deep learning methods fail to account for these challenges. Existing generative and RL models lack mechanisms to enforce critical geometric and manufacturing constraints, including self-connectivity, symmetry, periodic compatibility, and printability. Moreover, no existing approach incorporates defect-aware design – the ability to explicitly account for fabrication-induced imperfections – which limits the reliability and real-world applicability of the generated metamaterials.

To address these challenges, we introduce GraphMetaMat, a graph-based inverse design framework that leverages a graph neural network (GNN) agent to autoregressively generate 3D truss metamaterials with prescribed nonlinear responses. A response-to-structure policy network, guided by a physics-informed structure-to-response surrogate model and Monte Carlo Tree Search (MCTS), is trained using deep imitation learning (IL) and RL. This unified framework enables inverse design under strict geometric and manufacturing constraints – including symmetry, periodic compatibility, printability, and, critically, defect tolerance. GraphMetaMat uniquely incorporates fabrication-induced imperfections such as missing struts, delamination, and geometric non-uniformities into the design process, addressing a major gap in prior generative models.

As a proof of concept in mechanical metamaterials, we focus on inverse design of compressive stress-strain and vibration transmission curves, which arise from complex physical phenomena such as buckling, frictional contact, and wave propagation. GraphMetaMat efficiently generates manufacturable designs with stress responses spanning four orders of magnitude and tailored acoustic attenuation gaps. Enabled by its physics-informed forward model and graph representation, it can also identify and select designs with lower defect sensitivity. Applied to real-world problems, GraphMetaMat discovers lightweight structures with high energy absorption and low peak stress, or low vibration transmission – offering potential solutions for protective systems and noise mitigation in applications like electric vehicles. This framework paves the way for scalable, automated discovery of manufacturable, defect-tolerant metamaterials.

Results

Graph-response space

Translating truss metamaterials into graphs allows us to exploit the inductive biases of GNNs[52]. In 'graph space' (Fig. 1A-B), metamaterial struts and junctions (intersections between struts) are represented as edges (E) and nodes (V) of the graph $G(V, E)$, respectively. The *geometry*, including node coordinates, x_i and strut length, l_{ij}, is encoded into node (v_i) and edge (e_{ij}) features, for each node i, j. Here we assume uniform relative density, $\overline{\rho}$ across the metamaterial. Hence, $\overline{\rho}$ is not directly encoded through GNNs, but processed via MLPs and concatenated with graph embeddings, if needed. The *topology* of the metamaterial, i.e., which struts connect to each other, is captured by the graph connectivity, eliminating the need to parametrize the design space with pre-existing structures[30,50,53] or pre-selected building blocks[29,54].

To test our inverse design framework, we restricted the design space to cubic symmetric periodic truss metamaterials with cylindrical struts (Fig. 1C and Supplementary figs. S1-S7), similarly to ref.[55]. To ensure invariant mechanical responses along three orthogonal and diagonal directions, a cubic volume is decomposed into 48 tetrahedra, forming the 'smallest representative volumes' (SRVs). While alternative decompositions exist[51], they break the symmetry while offering no guarantee of achieving a wider range of functional responses (Supplementary Section 1.1). The corresponding graph is constructed in the SRV by placing nodes along its edges and connecting them to form a sequence (Fig. 1C). The struts' radius, r_{ij} is then obtained from the relative density, $\overline{\rho}$ sampled in the range 0.05 – 0.25, assuming a constant unit cell size, L. By varying nodes, node coordinates, connectivity, and relative density, a large pool of diverse designs can be generated (Fig. 1D). We emphasize that any 3D truss architecture, regardless of the constitutive material, can be represented as a graph, without restrictions to regular periodic[32,51,57] or two-dimensional structures[29,41,58]. However, cubic symmetry not only enhances isotropic behavior but also simplifies the generation of heterogeneous metamaterials by modifying only the interior nodes and connectivity (Supplementary fig. S8), eliminating the need for boundary node-matching methods[54]. Moreover, the chosen design space includes classical stretching- and bending-dominated lattices, such as octet and Kelvin foams, as well as bi-stable structures (Supplementary fig. S3). Further details are provided in Supplementary Section 1.

This potentially unlimited design space, while challenging, offers the opportunity to design metamaterials with a wide variety of functional responses. To train our framework, we collected ~ 3,000 graph-curve data points via high-fidelity FE simulations for quasi-static stress-strain and wave transmission responses (see Methods). Each graph represents a metamaterial with distinct geometry, topology, and relative density, generated by randomly selecting and connecting nodes on each SRV edge. The datasets ensure both geometric and response diversity, as shown in Supplementary figs. S6, S11, and S17. Figure 1E and F illustrate the corresponding dimensionless curve spaces, which define the design regions for our framework by upper and lower bounds (Supplementary Section 3.2), along with representative curves and graphs from our datasets. Using a single linear elastic constitutive material (Methods), multiple compressive responses – including strain hardening and softening (Supplementary figs. S11-S13) – emerge across four orders of magnitude (Supplementary figs. S15-S16) due to the interplay of large deformations, buckling, and frictional contact. Similarly, vibration transmission curves exhibiting complex features and variable attenuation gaps, ranging from -120 to 20 dB, arise from the interaction between architecture and relative density (Supplementary figs. S17-S21). Further details are provided in Supplementary Sections 2 and 3. This vast design space enables our framework to inverse design target functional responses, spanning orders of magnitude in stress and featuring complex transmission characteristics.

Autoregressive framework for constrained graph generation

Our inverse-design framework, GraphMetaMat, is illustrated in Fig. 2. To enforce geometric constraints during metamaterial generation, the design process in graph space is decomposed into an autoregressive Markov decision process, where edges are autoregressively added to the SRV graph, $G(V, E)$, trained using RL. At each generation step, the RL environment ensures that all desirable geometric properties, such as maximum number of graph nodes, $V_{\max}$, self-connectivity, and cell-to-cell connectivity (see next), and functional responses are satisfied. Specifically, the generation process starts at an initial state $s_0 = (G_0, \overline{y})$, which consists of the empty graph $G_0 = (\emptyset, \emptyset)$, and the target response $\bar{y}$. At each (pseudo-) time step k, the agent selects an action $a_k =$

$\big((u,v),S\big)$, composed of an edge $(u,v):u,v\in V$, and a Boolean stop token S. If the stop token is true, the search process ends. Otherwise, the selected edge is added to the previous graph: $G_{k+1}=(V_k\cup\{u,v\},E_k\cup\{(u,v)\})$. When the search process ends, the resulting SRV graph is tessellated into the metamaterial's unit cell graph, $\tilde{G}$.

We model the RL agent with a policy network, π_θ (Fig. 2A and Extended Data Fig. 1), conditioned on a target curve, $\overline{y}$. According to dataset generation (Supplementary Section 2), we discretize the possible node locations into 5 equidistant positions on each edge of the SRV. This introduces an action space of 22 possible locations across the SRV. At each autoregressive step, the policy network first encodes the current state, $s_k=(G_k,\overline{y})$ by running a graph encoder on the SRV graph G_k, a curve encoder on the input response $\overline{y}$, and merging them together with an MLP. Then, it decodes the state embedding by running three different MLPs to select the start node u, the end node v, and the stop token S. While the goal of the agent at each step is to choose an edge in the SRV, due to efficiency reasons, the policy network predicts two nodes. To resemble picking an edge, we condition the end node selection on the start node by concatenating the end node MLP's input with the graph encoder embedding of the chosen start node.

To ensure the generated metamaterial exhibits the desired response, the policy network is trained using a proximal policy optimization (PPO) scheme[59], aiming to maximize the future expected reward R. This is function of Jaccard, J which measures the similarity between the target response, $\overline{y}$ and the generated metamaterial's response, y. We highlight PPO is an unsupervised learning algorithm, greatly reducing the data costs for conditioning on new desired responses. Hence, any new response can be encoded through training a new response encoder (Supplementary Section 5.4). Because RL requires repeated reward computations, we use a trained GNN-based forward, i.e., structure-to-response, model (Extended Data Fig. 1) to efficiently predict the response of the inverse-designed metamaterials (Supplementary figs. S25-S26). This model employs snapshot ensembles[60] to efficiently estimate prediction uncertainty, guiding metamaterial generation through reward modeling with uncertainty (Supplementary Section 5.1) while balancing target matching and prediction confidence. Additionally, pretraining and physics bias are incorporated to enhance the forward model's generalizability. For stress-strain responses, we assume that the curve magnitude $y_{\max}$ scales with the relative density $\overline{\rho}$ through the topology-dependent coefficients C and n, following $y_{\max}=C\overline{\rho}^{n}$ (ref.[7]) (Supplementary Section 4 for details). The model predicts these coefficients, enabling GraphMetaMat to reconstruct stress-strain curves across four orders of magnitude and generalize to unseen relative densities. During inverse design, due to the large effect of relative density, we test 16 evenly spaced relative densities between the upper and lower bound densities (constraint) and pick the best performing $\overline{\rho}$ according to the reward (Supplementary Section 5.1). Furthermore, to improve model performances (Extended Data Fig. 2), the policy network is pretrained using IL to learn the correct sequence of actions, $\{a_0,\dots,a_K\}$ for graph-labeled training target curves. Graph generation during RL training is shown in Supplementary Videos 1-2 for two validation target responses.

GraphMetaMat's inference process uses powerful search algorithms to discover high-quality truss graph representations. Specifically, we use MCTS rollouts to estimate the value of each state s_k in a search tree by sampling each action $a_{k+1}\sim\pi_\theta(\cdot\,|s_k)$ from its probability distribution over actions. The model iteratively samples multiple generated graphs and selects the best one from 128 iterations, significantly improving inverse design performance (Extended Data Fig. 2). As a final validation step, the corresponding structure is 3D-printed and tested (Fig. 2D).

As opposed to state-of-the-art inverse-design methods[28,50,51], GraphMetaMat allows for flexible enforcement of geometric constraints (Fig. 2B). In this work, symmetry is first constrained by

design through the SRV graph. Second, we constrain the relative density into the arbitrary ranges 0.05 – 0.25 and 0.02 – 0.25 (see next). Third, the maximum number of SRV graph nodes, $V_{\max}$ is limited to 4 to reduce data requirements and possible edge intersections not explicitly modeled during RL. Lastly, all generated graphs are physically viable by enforcing self-connectivity, and cell-to-cell connectivity (Fig. 2B). These constraints are satisfied by masking possible actions (Supplementary Section 5.3). Depending on the design space, different constraints can be imposed in GraphMetaMat. We highlight that manufacturing constraints can also be easily included. Fig. 2B (right panel) shows how the position of a single node in the SRV graph can determine printability, intended as in ref.[55] (Supplementary Section 5.3). Printability depends on the final graph rather than on the single predicted graph nodes. Therefore, to enforce printability on each action, all possible sequences of actions that enable printable structures must be known beforehand. While feasible in 2D, the extension to 3D graphs becomes intractable. To overcome this challenge and to make the solution more general, GraphMetaMat can employ an additional reward term, R_{supp} measuring the fraction of supported nodes, acting as a weak constraint (Supplementary Section 5.3). As a result, the generated structure, while still matching the target response, only needs a few additional (Extended Data Fig. 3) or no supports at all (Fig. 2C) to be printable. Employing a Markov decision process guided by an autoregressive policy network thus enables to design truss metamaterials with arbitrary geometric constraints, pivotal in the 'design for manufacturing' of architected materials. Complete technical details of GraphMetaMat, detailed ablation studies (Extended Data Figs. 2-3 and Supplementary fig. S38), and comparisons with state-of-the-art methods (Supplementary figs. S40-49) are provided in Supplementary Section 4 – 7.

Inverse design of unseen and user-defined nonlinear responses

We demonstrate GraphMetaMat ability to inverse-design truss metamaterials with target nonlinear responses and geometric constraints by considering two classes of unseen compressive stress-strain and vibration transmission curves. To the first class belong curves with known associated structures yet unseen during training (test dataset), here defined as 'known curve space'. User-defined responses, where the existence of an associated structure is not guaranteed, represent the second class of target curves, here defined as 'unknown curve space'. While the first is useful to assess model performance, the second class pushes the limits of the model.

We plot the forward model predictions, the closest curve from the training dataset (best train match), and the FE-reconstructed responses of three generated designs for representative compressive target curves from the unknown curve space in Fig. 3A. Three types of target curves are considered: (i) stronger than any training curve with an elastic perfect-plastic-like behavior, (ii) stronger than any training curve with a strain-hardening-like behavior, and (iii) softer than the most compliant structure in the dataset (Methods). The model successfully captures both the shape and magnitude of the target curves for (i) and (ii), achieving errors that are $1/6$ and $1/2$ of those from the best train match, respectively. Notably, while the generated designs have a lower relative density than the best train match, they exhibit a higher maximum stress. This demonstrates that although $\overline{\rho}$ significantly influences the curve's magnitude, GraphMetaMat enables the design of out-of-distribution curves by carefully adjusting the graph topology. Furthermore, enabled by the metamaterial-specific physics-informed forward GNN, GraphMetaMat can extend the $\overline{\rho}$ search down to 2 %, allowing it to design structures with substantially lower out-of-distribution stress, outperforming the best train match by approximately 30 times. Similar plots are shown in Extended Data Fig. 4A for targets sampled from the known curve space. The model can capture strain-

hardening due to self-contact, perfect-plasticity-like and softening due to buckling, with relative errors (NMAE; see Methods) between the FE-reconstructed and target curves of $5-6$ % (~ 10 % in average out of 100 test responses; Supplementary figs. S30-S32). These errors are close to the mismatch between the forward-predicted and target responses (Supplementary Section 5.8), proving GraphMetaMat ability to accurately inverse-design unseen curves with complex shapes.

Defining realistic target transmission curves is far more challenging than shaping realistic stress-strain responses, and applications often require metamaterials with specific attenuation gaps (low transmission in certain frequency ranges) rather than exact transmission values. To this end, instead of targeting transmission curves $T(f)$, we target binary sequences defined by thresholding T with T_{th}, where '0' corresponds to 'low transmission' ($T < T_{th}$) and '1' to 'high transmission' ($T \geq T_{th}$). During RL training, the forward model still predicts the transmission curve, which is then binarized for comparison with the target sequence. We define three types of targets, (i), (ii), and (iii), with varying gap size Δf, from ~1.4 to 2.1 and 2.7 kHz, respectively. Fig. 3B highlights how GraphMetaMat can design structures with out-of-distribution target attenuation gaps, with variable central frequencies and gap size, outperforming best train matches (Supplementary figs. S34-36 for more examples). In Extended Data Fig. 4B, instead of targeting specific attenuation gaps, we design for transmission responses from the known curve space. Using a transmission threshold of $T_{\text{th}} = -10$ dB, we achieve ~ 95 % accuracy between the FE-reconstructed and target curves for these examples, demonstrating the model's ability to generate structures with unseen transmission profiles (Supplementary fig. S31). Across 100 test responses (Supplementary fig. S32D-E), we observe an average accuracy of ~72 %, and ~77 % when considering attenuation gaps (Methods) – both values fall within the typical mismatch between the forward-predicted and target curves.

An in-depth comparison with state-of-the-art inverse design methods[28,50,51] highlights the clear advantage of GraphMetaMat. MLP-based VAE and 3D conditional GAN approaches[45,51] fail to reconstruct our structures (Supplementary figs. S40 and S48) – a critical requirement for inverse design – limiting their use to data-intensive problems. This confirms that GraphMetaMat's performance stems not from a reduced design space, but from its integration of GNNs with physics biases, IL, RL, and MCTS, enabling operation in low-data regimes. MLP-based tandem networks[50], constrained by design vector parametrization, are unable to inverse design either test or user-defined stress-strain curves, with errors ranging from 30 to 100,000 % (Supplementary figs. S41-S42), even when using compound metamaterials to expand design diversity. When considering only the curve's shape, errors remain substantial, reaching up to 100 %. Notably, despite no imposed constraints on relative density (and thus strut radii), these models still fail, indicating that limited topological diversity and poor generalization, not beam size, are the primary bottlenecks. Furthermore, when benchmarked against denoising diffusion generative models[28], designed for 2D pixel-based structures, GraphMetaMat achieves an average 60% performance improvement, with peaks reaching a tenfold increase (Supplementary figs. S43-S46). Unlike GraphMetaMat, these models struggle to accurately capture nonlinear curves across a wide response range and fail to ensure the generation of valid, connected, and manufacturable structures (Extended Data Fig. 6 and Table 1 provide a summary). Comprehensive benchmark details are available in Supplementary Section 7.

Defect-aware metamaterials design

Manufacturing defects – such as missing struts, delamination, and non-uniformities (Fig. 4A) – significantly impact the response of metamaterials, making their consideration during design a

long-standing challenge[61–64]. Here, we demonstrate how GraphMetaMat, once trained, can seamlessly integrate never-seen defects into the inverse design process, automatically identifying and selecting designs with higher defect tolerance, a capability unattainable by previous methods.

Figures 4A–B illustrate three typical additive manufacturing defects and their corresponding graph representations. Periodic defects, such as missing struts, are modeled by randomly removing edges from the unit cell graph. Non-periodic defects, including delamination and non-uniformities, are captured within $M \times M \times M$ tessellations of the unit cell graph (here, $M = 2$, consistent with experiments). Delamination, typically occurring along planes orthogonal to the printing direction, is represented by selectively removing close-to-the-plane edges either randomly or locally (Fig. 4B and Supplementary fig. S51). Non-uniformities, such as strut radius variations, are directly incorporated into the forward model via a defect-aware message passing mechanism (Fig. 4C). In this post-training modified message passing, the message m_{ij} exchanged between nodes i and j is rescaled by a coefficient α_{ij}, which quantifies the defect intensity along the strut $i - j$. For a missing strut, α_{ij} is trivially zero, whereas for radius variations, α_{ij} represents the deviation from the nominal radius corresponding to the nominal relative density. Supplementary figs. S50–S52 validate GraphMetaMat on various defect types. For example, as the fraction of missing unit cell struts increases (Supplementary fig. S50), the model accurately predicts the resulting change in stress-strain response. The higher the similarity between the pristine and flawed design responses, the lower the defect sensitivity. Integrated into the inverse design workflow (Fig. 4C-D), the defect-aware message-passing, physics-informed GNN model enables the evaluation of defect tolerance in generated design candidates, selecting those with lower defect sensitivity (Extended Data Fig. 5). Further details are provided in Supplementary Section 8.

Generation of metamaterials with impact-protection and vibration-attenuation functions

To challenge our model, we applied GraphMetaMat to design cushioning metamaterial for lacrosse chest protectors and vibration-damping panels for electric vehicles (EV). Chest protectors are usually composed of stacked foam layers (Fig. 5B), here referred to as 'foams', designed to overall reduce the transmitted peak force. By using GraphMetaMat, we explored the possibility to design a single-material 3D-printed periodic metamaterial able to outperform commercial foams. To this end, using the measured average compressive response of foams as baseline, we targeted stress-strain curves with lower or same peak stress, $\sigma_{\max}$ and higher energy absorption, U (Fig. 5A-B; Methods). To reduce the cost of high strain-rate training data collection, we first targeted quasi-static responses with our model (Fig. 5A-D and Supplementary fig. S55) and verified the results with dynamic impact simulations (Supplementary fig. S56E-G). Restricting the design to $\overline{\rho}$ between 5 and 10 %, Fig. 5B and C report an example of generated 3D-printed metamaterial with corresponding experimental stress-strain curve. We benchmark the generated design with the baseline foams and two classical 3D periodic structures – Kelvin and octet. The performance summary in Fig. 5D indicates the generated design has a limited peak stress, close to that of Kelvin and commercial foams, yet $\sim 25 - 75$ % higher energy absorption, despite its apparent structural simplicity. The curves and FE-deformed shapes of the samples (Fig. 5C) demonstrate these results emerge from the interplay between higher stiffness, caused by struts aligned along the loading direction, increasing the energy absorption, and local buckling, limiting the peak stress. Details are reported in Supplementary Section 9.

Although electric motors are generally quieter than internal combustion engines, the pure tonal noise at frequencies above 1 kHz generated by electromagnetic forces is perceived as more

annoying[65] (Supplementary fig. S57A-B). In the frequency range 1 – 12 kHz, GraphMetaMat can design structures with a large diversity of vibration attenuation gaps (Fig. 5E). By exploiting this capability, we targeted a broadband attenuation gap in the whole frequency range. Fig. 5H shows the 3D-printed designed metamaterial with broadband low transmission response, benchmarked with a state-of-the-art 3D-printed metamaterial optimized for broadband vibration filtering[66] (Supplementary fig. S57E-F for other benchmarks). Two observations can be made. First, while the benchmark has an attenuation gap only for $f > 4$ kHz, the generated design exhibits a broadband attenuation with transmission values below -20 dB at all frequencies. Second, the generated design is ~86 % lighter than the benchmark. In our dataset, we noticed lighter structures are correlated with low-transmission responses (Supplementary figs. S17 and S20-S21). This may explain why GraphMetaMat tends to favor lightweight designs for broadband attenuation gaps. Nevertheless, relative density alone does not guarantee full control over transmission response (Supplementary fig. S19). The design of metamaterials with tunable transmission is indeed enabled by the simultaneous control of topology and relative density. Details are reported in Supplementary Section 10.

Discussion

Designing metamaterials with programmable functional responses addresses the need for customizable materials. In this work, we introduced GraphMetaMat, a graph-based autoregressive framework for inverse designing truss metamaterials with diverse functional responses and arbitrary geometric constraints. This framework admits extension to any graph-representable metamaterials, including recently formulated shell-based structures[67], and functional responses, from thermal to optical and piezoelectric. Compared to graph-based generative models – such as GANs[48], VAEs[49], and diffusion models[35,36] – as well as prior metamaterial inverse design frameworks[28,29,31,47,50,51,68], GraphMetaMat offers several key advantages. Through reinforcement learning, it explicitly imposes structural constraints, including self-connectivity, cell-to-cell connectivity, and manufacturability, ensuring valid designs. Leveraging GNNs and physics biases, it can handle any graph-based metamaterial, regardless of topology or size, while capturing complex nonlinear physics. By integrating GNNs, physics biases, IL, RL, and MCTS, GraphMetaMat conditionally generates graphs using only a few thousand training samples, while effectively generalizing beyond the training data. Through a defect-aware message-passing, physics-informed forward GNN model, GraphMetaMat generalizes to never-seen manufacturing defects, such as missing struts, delamination, and non-uniformities, automatically identifying and selecting designs with lower defect sensitivity. At inference time, it can efficiently generate hundreds of valid structures with different target responses without relying on costly gradient-based optimization. Furthermore, it provides control over both topology and relative density, enabling a broad design-response space. See Extended Data Fig. 6 and Table 1 for a summary benchmark between GraphMetaMat and state-of-the-art methods.

In this work, we focused on the inverse design of structures for single target responses, such as compressive and vibrational curves. As a by-product, GraphMetaMat enabled multi-objective optimization of derived properties, including peak stress and energy absorption from stress-strain curves. In principle, the framework can be extended to the simultaneous design of multiple, potentially competing responses. For example, achieving both structural support and broadband vibration attenuation requires maximizing stiffness (the slope of the stress-strain curve) while minimizing vibration transmission. This, however, would require additional training data and the adoption of multi-objective RL schemes[69]. Since multi-objective RL depends on accurately

characterizing the Pareto front, it demands a more precise reward signal from the forward model, which is currently limited by the availability of high-fidelity data. Multi-fidelity transfer learning[70] could alleviate this bottleneck, reducing computational costs and improving reward accuracy – thus paving the way for effective multi-objective design. Further, incorporating flawed structures into the training data, such as variations in base material properties and experimentally observed delamination, could enhance defect-awareness and improve generalization to real-world manufacturing imperfections. Finally, GraphMetaMat offers a new platform extendable to the design of architected robotic matter[1,71], where defect tolerance and strict geometric and manufacturing constraints pose extreme challenges for its industrial deployment.

Methods

Finite element simulations

The stress-strain and elastic wave transmission responses were collected via high-fidelity finite element (FE) simulations. The stress-strain and transmission simulations were fully automated using Python scripting in Abaqus/CAE 2018, and the MPh Python package to interface with COMSOL Multiphysics 6.0, respectively. Custom scripts generated each simulation file from scratch, defining geometry, material properties, boundary conditions, meshing, and loading. Due to model complexity, each simulation averaged one hour to complete. Utilizing three dedicated workstations – AMD Ryzen 3960X, AMD Ryzen 9 7950X, and AMD Ryzen 9 5950X – we generated full datasets of ~3,000 simulations each over two months. This automation ensured consistency and reproducibility. To reduce the computational cost of training data collection, $2 \times 2 \times 2$ periodic metamaterials were simulated under quasi-static and dynamic vibration excitations (see Supplementary figs. S12-S13 for a sensitivity analysis on $M \times M \times M$ tessellations with $M > 2$).

Stress-strain

To collect the stress-strain curves, we performed quasi-static compressive simulations of the metamaterials between two rigid plates. The structure is constrained to the bottom and top plate, while a vertical displacement u^* is applied to the top plate, corresponding to the final macroscopic strain ε_{max} via $u^* = \varepsilon_{max} ML$. ML corresponds to the initial height of the structure, with L being the unit cell size, and M the number of unit cells. In our case, $M = 2$, and $L = 10$ mm. It is crucial to note that our inverse design framework is scale independent as far as the training data are consistent with the constitutive material's behavior. The stress is computed as F/A where F is the total reaction force measured at the bottom plate, and $A = ML \times ML$ is the cross-sectional area of the lattice. The applied strain is computed as $\varepsilon = u/(ML)$, where u corresponds to the applied displacement on the top plate. As a post-processing phase, the collected responses are filtered to remove high-frequency numerical oscillations. The constitutive material is modeled as linear elastic with Young's modulus $E_s = 4.0\ MPa$, and Poisson's ratio $\nu_s = 0.3$, with properties of the Formlabs Flexible 80A material. Owing to its large strain at failure, fracture of the constitutive material is not here considered (see Methods 'Constitutive materials characterization'). Abaqus/Explicit is employed to simulate the structures up to 30 % of strain. Quasi-static conditions are ensured by limiting the kinetic energy within 1 % of the internal energy. Geometric nonlinearities and frictionless contact are modeled. The structures are meshed using four-node tetrahedral elements (C3D4 in Abaqus) with average size $2r$, where r is the strut's radius, depending on the structure and relative density. A mesh sensitivity analysis was performed to

balance accuracy and speed. Strength and stiffness of metamaterials are defined as the peak stress and slope of the curve at $\varepsilon = 0.1$ %, respectively.

Wave transmission

The transmission curves were obtained via vibration simulations using the Solid Mechanics module in COMSOL Multiphysics 6.0. To resemble application conditions and to ensure experimental reproducibility, lattice-cored sandwich structures are considered, meaning the plates are not rigid but modeled with the same constitutive material (Supplementary fig. S10A). As before, we set unit cell size $L = 10$ mm and tessellation of unit cells $M = 2$. A sinusoidal excitation force is applied on the bottom plate within a 4.5 mm radius circular region, matching the shaker contact area in the experimental setup (see Supplementary fig. S10B and Methods 'Mechanical Testing'). A harmonic frequency sweep is performed in the range of 1–12 kHz. The wave transmission curve along the excitation direction, measured in decibel (dB), is then calculated by $20\log_{10}(u_{out}/u_{in})$, where u_{in} is the input displacement averaged over the shaker contact area and u_{out} is the output displacement at the center point of the top plate. This output displacement corresponds to the displacement measured by the laser vibrometer (LDV) during experimental testing. The constitutive material, TMPTA, is modeled as viscoelastic with frequency-dependent storage Young's modulus $E_s'(f)$, and loss factor $\tan(\delta)(f)$, constant Poisson's ratio $\nu_s = 0.3$, and density $\rho_s = 1050\,\mathrm{kg/m^3}$. (see Methods 'Constitutive materials characterization'). The structures are meshed using four-node tetrahedral elements with minimum and maximum size R and $2R$, respectively, where R is the strut's radius, depending on the structure and relative density. A mesh sensitivity analysis was performed to balance accuracy and speed. As a post-processing phase, in agreement with our measurement system, noise floor was set to -40 dB, making the transmission responses flat for values below -40 dB.

GraphMetaMat

The proposed inverse-design framework is implemented in Python 3.9, within the PyTorch environment. Details and explanations are reported in the Supplementary Section 4 and 5.

Target responses

Stress-strain

The user-defined target curves presented in Fig. 3A are designed to ensure a diverse set of out-of-distribution responses, for which the corresponding structures are not known a priori. Curves (i) and (ii) represent stronger responses, resembling elastic perfect-plastic and strain-hardening behaviors, respectively, and are generated by rescaling existing dataset curves. To assess GraphMetaMat's ability to inverse design structures with higher stress magnitudes, we trained the model on a different dataset split, consisting of structures with peak stress values below a specified threshold. This threshold was adjusted to ensure a sufficient number of training graph-curve pairs. Curves of type (iii) represent softer responses, defined by $\sigma = kE_{\mathrm{soft}}\varepsilon$, where $k \in [0.1, 0.9]$ and E_{soft} is the stiffness of the most compliant structure in the dataset. A total of 40,000 curves were generated for training and testing the inverse model by linearly sampling k with 10,000 points for each curve type. To help the model find possible designs when targeting curves of type (iii), we extend $\overline{\rho}$ search down to 0.02.

The application-oriented target curve shown in Fig. 5A addresses the need for higher energy absorption and lower peak stress by mimicking an elastic perfect-plastic behavior. To conduct

ablation studies using application-oriented target curves (Extended Data Fig. 2), we used the quasi-static compressive response of foams in commercial chest protectors as a baseline. A total of 5,000 curves were generated by varying peak stress reduction within the range of 5 – 30% and energy absorption increase within 0 – 20%. Given an energy absorption gain, i.e., a larger area under the curve, the stiffness of the structure is adjusted accordingly for each peak stress reduction.

Wave transmission

The target binary sequences shown in Fig. 3B are constructed to inverse design metamaterials with tunable attenuation gaps, i.e., low transmission $T(f)$ in specific frequency ranges. The vector sequences are generated by first discretizing the frequency range into 16 intervals, and initializing the vectors with '1's. Then, two attenuation gaps, i.e., parts of the vectors filled with '0's, of size $0 < n < 8$, are randomly dispersed into the sequences without overlapping. The gaps have a frequency size $\Delta f = \frac{n}{16} * 11$ kHz. By varying n, we construct three types of sequences (i), (ii), and (iii), with $\Delta f \sim 1.4, 2.1, 2.7$ kHz, respectively. 55, 28, and 10 sequences were generated for type (i), (ii), and (iii), respectively.

The application-oriented target gaps in Fig. 5E to H correspond to constant transmission responses from 5 down to – 40 dB, in the frequency range 1 – 12 kHz. In total, we generated 1,000 curves for training and testing our framework. With these target curves, we aim at challenging GraphMetaMat to design structures with tunable attenuation gaps, from small frequency gap at high frequencies (Fig. 5F) to broadband vibration filtering in the whole frequency range (Fig. 5H).

Error metrics

To measure the performance of GraphMetaMat on the stress-strain responses we adopt an objective and scale-invariant relative error, the normalized mean absolute error (NMAE):

$$\text{NMAE} = \frac{|y - \overline{y}|}{\overline{y}_{\max} - \overline{y}_{\min}} \times 100, \quad (1)$$

where y is either the predicted or FE-reconstructed response, and $\overline{y}$ is the target response. By replacing the target response with the ground-truth curve, the same metric is used for the forward model.

For transmission responses, we adopt the accuracy on the binarized sequence defined as the fraction of correct predictions on the whole sequence, and the accuracy on the attenuation gaps ('0' values in the binarized sequence) defined as the fraction of correctly predicted attenuation gaps. These metrics are used both on target curves (such as test curves in Extended Data Fig. 4B) and binary sequences (such as user-defined sequences in Fig. 3B).

Sample fabrication

Samples were fabricated by using a digital light 3D-printer Anycubic Photon Ultra and D2 (ANYCUBIC Technology Co., Ltd) for compressive and transmission response design, respectively. To reach large deformations without catastrophic failure, the samples for quasi-static compressive responses are made of a commercial photosensitive resin, Flexible 80A (Formlabs Inc., Somerville, MA). To improve printability, we added 0.0125wt% photoabsorber to it. With this resin, slice thickness and exposure time were set to 0.050 mm and 15 s, respectively. To reduce the viscoelastic damping effect at higher frequencies, the samples for vibration transmission responses are made of a brittle material, denoted as TMPTA. This latter is an in-house photosensitive resin composed of trimethylolpropane triacrylate (Sigma–Aldrich Inc., St. Louis,

MO) with 0.0125wt% photoabsorber and 2wt% phenylbis(2,4,6-trimethylbenzoyl) phosphine oxide photoinitiator (Sigma–Aldrich Inc., St. Louis, MO). With this resin, slice thickness and exposure time are set to 0.040 mm and 5 s, respectively. To balance 3D-printing resolution and printing volume, all samples are fabricated with a unit cell size of 10 mm. After fabrication, all samples are cleaned with ethanol and dried in a dark environment for at least 24 hours.

Constitutive materials characterization

For quasi-static properties, dog-bone samples made of flexible resin (Flexible 80A) were fabricated employing the same printer and printing parameters used for the lattice samples. The samples were tested under quasi-static uniaxial tensile loading using a universal testing machine, Instron 5944 (Instron Corporation, Norwood, MA). The strain rate was set to $10^{-3}\mathrm{s}^{-1}$. Supplementary fig. S9A-B shows the resulting stress-strain curves for three different printing directions. Although a certain degree of anisotropy is found for strength and strain at failure, based on experimental observations (Supplementary fig. S55A), we assume our structures will not fail up to 30 % of macroscopic strain. Accordingly, a linear elastic material model with $E_s = 4$ MPa is fitted on these data.

Dynamic mechanical analysis (DMA, Q800 model, TA Instruments; Supplementary fig. S9D) was used to characterize the viscoelastic properties of the material TMPTA, including the storage modulus E_s' and the loss modulus (E_s''). The loss factor, $\tan(\delta)$, which is the ratio between E_s'' and E_s', was also obtained. Specimens with dimensions of 25 mm length, 8 mm width, and 1 mm thickness were used for DMA measurements. A dynamic displacement with an oscillation amplitude of 5 μm was applied to the specimens over a frequency range of 0.1 Hz to 100 Hz, with 16 points sampled on a logarithmic scale. The measurements were conducted at temperatures ranging from -2°C to 22°C, with intervals of 3°C. The time-temperature superposition (TTS) principle was used to estimate the master curve by shifting each measured isotherms along the frequency axis to align with the selected reference temperature of 22°C [72]. Master curves for E_s'', E_s' and the corresponding $\tan(\delta)$ were obtained from 0.1 Hz to 10 kHz (Supplementary fig. S9E-G) and were then used for modeling the transmission curve in COMSOL. At least three samples per constitutive material were tested.

Mechanical testing

All quasi-static compression tests were performed by using a universal testing machine, Instron 5944 (Instron Corporation, Norwood, MA). The samples are compressed between the stationary and moving steel plates. To resemble the boundary conditions used in the training dataset, the samples are fixed on the two plates. Force-displacement curves are measured by the Instron load cell with a maximum capacity of 2000 N and the built-in crosshead encoder. Stress-strain curves are computed analogously to what is done for FE simulations. The strain rate for all tests is set to $10^{-3}\mathrm{s}^{-1}$.

Vibration tests were performed by using an electrodynamical shaker, LDS (Ling Dynamic Systems, Ltd, UK), and a laser scanning vibrometer Polytec PSV-500 (Polytec Inc.). The sample is fixed to the shaker using a clear epoxy (Devcon). As schematically reported in Supplementary fig. S10B, to vertically excite the samples, a sine sweep voltage, from 500 to 12500 Hz, is applied to the shaker. The following parameters were used: total sweep time of 65.54 s, amplitude voltage 5 V, FFT measurement mode with average of the magnitude on three measurements, sampling frequency 31.25 kHz, and frequency resolution ~15 mHz. The laser vibrometer is used to measure the acceleration spectrum $A(f)$ of a vibrating point. We first measure the acceleration of the shaker

$A_{\text{shaker}}(f)$ without any sample. Then, to resemble the boundary conditions used in the training dataset (Supplementary fig. S10A), we measure the acceleration of the center point of the top plate of the sample $A_{\text{structure}}(f)$. From the definition of wave transmission, we finally compute the transmission response as $T(f) = A_{\text{structure}}(f)/A_{\text{shaker}}(f)$, where $A_{\text{shaker}}(f)$ represents the acceleration input to structure's bottom plate. The noise floor of the system is around -40 dB. For quasi-static compression and vibration tests, at least three samples per structure were tested.

Data availability

All training and test datasets can be accessed in the GraphMetaMat-Datasets repository.

Code availability

The code developed in this study is available in the GitHub repository, GraphMetaMat-Code.

References

1. Cui, H. *et al.* Design and printing of proprioceptive three-dimensional architected robotic metamaterials. *Science* **376**, 1287–1293 (2022).
2. Bauer, J. *et al.* Nanolattices: An Emerging Class of Mechanical Metamaterials. *Advanced Materials* **29**, 1701850 (2017).
3. Filipov, E. T., Tachi, T. & Paulino, G. H. Origami tubes assembled into stiff, yet reconfigurable structures and metamaterials. *Proc. Natl. Acad. Sci. U.S.A.* **112**, 12321–12326 (2015).
4. Portela, C. M. *et al.* Supersonic impact resilience of nanoarchitected carbon. *Nat. Mater.* **20**, 1491–1497 (2021).
5. Schaedler, T. A. *et al.* Ultralight Metallic Microlattices. *Science* **334**, 962–965 (2011).
6. Xia, X., Spadaccini, C. M. & Greer, J. R. Responsive materials architected in space and time. *Nat Rev Mater* **7**, 683–701 (2022).
7. Ashby, M. F. The properties of foams and lattices. *Phil. Trans. R. Soc. A.* **364**, 15–30 (2006).
8. Zheng, X. *et al.* Ultralight, ultrastiff mechanical metamaterials. *Science* **344**, 1373–1377 (2014).
9. Meza, L. R., Das, S. & Greer, J. R. Strong, lightweight, and recoverable three-dimensional ceramic nanolattices. *Science* **345**, 1322–1326 (2014).
10. Meier, T. *et al.* Obtaining auxetic and isotropic metamaterials in counterintuitive design spaces: an automated optimization approach and experimental characterization. *npj Comput Mater* **10**, 3 (2024).

11. Xu, S., Shen, J., Zhou, S., Huang, X. & Xie, Y. M. Design of lattice structures with controlled anisotropy. *Materials & Design* **93**, 443–447 (2016).
12. Cui, H. *et al.* Three-dimensional printing of piezoelectric materials with designed anisotropy and directional response. *Nature Mater* **18**, 234–241 (2019).
13. Cheung, K. C. & Gershenfeld, N. Reversibly Assembled Cellular Composite Materials. *Science* **341**, 1219–1221 (2013).
14. Gregg, C. E. *et al.* Ultralight, strong, and self-reprogrammable mechanical metamaterials. *Sci. Robot.* **9**, eadi2746 (2024).
15. Woodman, S. J., Moore, A., Tagare, S., Cheung, K. & Kramer-Bottiglio, R. Deployable Cuboctahedrons for Adaptive Space Infrastructure. in *2024 IEEE 7th International Conference on Soft Robotics (RoboSoft)* 75–81 (IEEE, San Diego, CA, USA, 2024). doi:10.1109/RoboSoft60065.2024.10521988.
16. Huang, Z., Panozzo, D. & Zorin, D. Optimized shock-protecting microstructures. Preprint at https://doi.org/10.48550/ARXIV.2310.08609 (2023).
17. Yang, D. *et al.* Buckling of Elastomeric Beams Enables Actuation of Soft Machines. *Advanced Materials* **27**, 6323–6327 (2015).
18. Gerard, N. J. *et al.* Three-Dimensional Trampolinelike Behavior in an Ultralight Elastic Metamaterial. *Phys. Rev. Applied* **16**, 024015 (2021).
19. Bastek, J.-H., Kumar, S., Telgen, B., Glaesener, R. N. & Kochmann, D. M. Inverting the structure–property map of truss metamaterials by deep learning. *Proc. Natl. Acad. Sci. U.S.A.* **119**, e2111505119 (2022).
20. Kumar, S., Tan, S., Zheng, L. & Kochmann, D. M. Inverse-designed spinodoid metamaterials. *npj Comput Mater* **6**, 73 (2020).
21. Li, B. *et al.* Computational discovery of microstructured composites with optimal stiffness-toughness trade-offs. *Sci. Adv.* **10**, eadk4284 (2024).
22. Liu, H. *et al.* De Novo Atomistic Discovery of Disordered Mechanical Metamaterials by Machine Learning. *Advanced Science* **11**, 2304834 (2024).
23. Luan, S., Chen, E., John, J. & Gaitanaros, S. A data-driven framework for structure-property correlation in ordered and disordered cellular metamaterials. *Sci. Adv.* **9**, eadi1453 (2023).

24. Mao, Y., He, Q. & Zhao, X. Designing complex architectured materials with generative adversarial networks. *Sci. Adv.* **6**, eaaz4169 (2020).
25. Shen, S. C. & Buehler, M. J. Nature-inspired architected materials using unsupervised deep learning. *Commun Eng* **1**, 37 (2022).
26. Van 'T Sant, S., Thakolkaran, P., Martínez, J. & Kumar, S. Inverse-designed growth-based cellular metamaterials. *Mechanics of Materials* **182**, 104668 (2023).
27. Zheng, L., Kumar, S. & Kochmann, D. M. Data-driven topology optimization of spinodoid metamaterials with seamlessly tunable anisotropy. *Computer Methods in Applied Mechanics and Engineering* **383**, 113894 (2021).
28. Bastek, J.-H. & Kochmann, D. M. Inverse design of nonlinear mechanical metamaterials via video denoising diffusion models. *Nat Mach Intell* **5**, 1466–1475 (2023).
29. Maurizi, M., Gao, C. & Berto, F. Inverse design of truss lattice materials with superior buckling resistance. *npj Comput Mater* **8**, 247 (2022).
30. Lew, A. J., Jin, K. & Buehler, M. J. Designing architected materials for mechanical compression via simulation, deep learning, and experimentation. *npj Comput Mater* **9**, 80 (2023).
31. Thakolkaran, P., Espinal, M. A., Dhulipala, S., Kumar, S. & Portela, C. M. Experiment-informed finite-strain inverse design of spinodal metamaterials. Preprint at https://doi.org/10.48550/ARXIV.2312.11648 (2023).
32. Indurkar, P. P., Karlapati, S., Shaikeea, A. J. D. & Deshpande, V. S. Predicting deformation mechanisms in architected metamaterials using GNN. (2022) doi:10.48550/ARXIV.2202.09427.
33. Zhou, Z., Kearnes, S., Li, L., Zare, R. N. & Riley, P. Optimization of Molecules via Deep Reinforcement Learning. (2018) doi:10.48550/ARXIV.1810.08678.
34. Simm, G. N. C., Pinsler, R., Csányi, G. & Hernández-Lobato, J. M. Symmetry-Aware Actor-Critic for 3D Molecular Design. (2020) doi:10.48550/ARXIV.2011.12747.
35. Xu, M., Powers, A., Dror, R., Ermon, S. & Leskovec, J. Geometric Latent Diffusion Models for 3D Molecule Generation. Preprint at https://doi.org/10.48550/ARXIV.2305.01140 (2023).
36. Zhou, C., Wang, X. & Zhang, M. Unifying Generation and Prediction on Graphs with Latent Graph Diffusion. Preprint at https://doi.org/10.48550/arXiv.2402.02518 (2024).
37. Zeni, C. *et al.* A generative model for inorganic materials design. *Nature* **639**, 624–632 (2025).

38. Du, W. *et al.* Automatic Truss Design with Reinforcement Learning. in *Proceedings of the Thirty-Second International Joint Conference on Artificial Intelligence* 3659–3667 (International Joint Conferences on Artificial Intelligence Organization, Macau, SAR China, 2023). doi:10.24963/ijcai.2023/407.
39. Luo, R., Wang, Y., Liu, Z., Xiao, W. & Zhao, X. A Reinforcement Learning Method for Layout Design of Planar and Spatial Trusses using Kernel Regression. *Applied Sciences* **12**, 8227 (2022).
40. Kupwiwat, C., Hayashi, K. & Ohsaki, M. Multi-objective optimization of truss structure using multi-agent reinforcement learning and graph representation. *Engineering Applications of Artificial Intelligence* **129**, 107594 (2024).
41. Dold, D. & Aranguren Van Egmond, D. Differentiable graph-structured models for inverse design of lattice materials. *Cell Reports Physical Science* **4**, 101586 (2023).
42. Zheng, X., Zhang, X., Chen, T. & Watanabe, I. Deep Learning in Mechanical Metamaterials: From Prediction and Generation to Inverse Design. *Advanced Materials* **35**, 2302530 (2023).
43. Lee, D., Chen, W. (Wayne), Wang, L., Chan, Y. & Chen, W. Data-Driven Design for Metamaterials and Multiscale Systems: A Review. *Advanced Materials* **36**, 2305254 (2024).
44. Zheng, X., Chen, T.-T., Guo, X., Samitsu, S. & Watanabe, I. Controllable inverse design of auxetic metamaterials using deep learning. *Materials & Design* **211**, 110178 (2021).
45. Zheng, X., Chen, T.-T., Jiang, X., Naito, M. & Watanabe, I. Deep-learning-based inverse design of three-dimensional architected cellular materials with the target porosity and stiffness using voxelized Voronoi lattices. *Science and Technology of Advanced Materials* **24**, 2157682 (2023).
46. Wang, L. *et al.* Deep generative modeling for mechanistic-based learning and design of metamaterial systems. *Computer Methods in Applied Mechanics and Engineering* **372**, 113377 (2020).
47. Yang, Y. *et al.* Guided Diffusion for Fast Inverse Design of Density-based Mechanical Metamaterials. Preprint at https://doi.org/10.48550/ARXIV.2401.13570 (2024).
48. Wang, H. *et al.* GraphGAN: Graph Representation Learning With Generative Adversarial Nets. *AAAI* **32**, (2018).
49. Liu, Q., Allamanis, M., Brockschmidt, M. & Gaunt, A. L. Constrained Graph Variational Autoencoders for Molecule Design. Preprint at https://doi.org/10.48550/ARXIV.1805.09076 (2018).

50. Ha, C. S. *et al.* Rapid inverse design of metamaterials based on prescribed mechanical behavior through machine learning. *Nat Commun* **14**, 5765 (2023).
51. Zheng, L., Karapiperis, K., Kumar, S. & Kochmann, D. M. Unifying the design space and optimizing linear and nonlinear truss metamaterials by generative modeling. *Nat Commun* **14**, 7563 (2023).
52. Xu, K., Hu, W., Leskovec, J. & Jegelka, S. How Powerful are Graph Neural Networks? Preprint at https://doi.org/10.48550/ARXIV.1810.00826 (2018).
53. Lew, A. J. & Buehler, M. J. Single-shot forward and inverse hierarchical architected materials design for nonlinear mechanical properties using an Attention-Diffusion model. *Materials Today* **64**, 10–20 (2023).
54. Liu, K., Sun, R. & Daraio, C. Growth rules for irregular architected materials with programmable properties. *Science* **377**, 975–981 (2022).
55. Panetta, J. *et al.* Elastic textures for additive fabrication. *ACM Trans. Graph.* **34**, 1–12 (2015).
56. Meza, L. R. *et al.* Reexamining the mechanical property space of three-dimensional lattice architectures. *Acta Materialia* **140**, 424–432 (2017).
57. Makatura, L. *et al.* Procedural Metamaterials: A Unified Procedural Graph for Metamaterial Design. *ACM Trans. Graph.* **42**, 1–19 (2023).
58. Maurizi, M., Gao, C. & Berto, F. Predicting stress, strain and deformation fields in materials and structures with graph neural networks. *Sci Rep* **12**, 21834 (2022).
59. Schulman, J., Wolski, F., Dhariwal, P., Radford, A. & Klimov, O. Proximal Policy Optimization Algorithms. (2017) doi:10.48550/ARXIV.1707.06347.
60. Huang, G. *et al.* Snapshot Ensembles: Train 1, get M for free. (2017) doi:10.48550/ARXIV.1704.00109.
61. Pasini, D. & Guest, J. K. Imperfect architected materials: Mechanics and topology optimization. *MRS Bull.* **44**, 766–772 (2019).
62. Glaesener, R. N. *et al.* Predicting the influence of geometric imperfections on the mechanical response of 2D and 3D periodic trusses. *Acta Materialia* **254**, 118918 (2023).
63. Ziemke, P. *et al.* The defect sensitivity of brittle truss-based metamaterials. *Materials & Design* **239**, 112776 (2024).
64. Symons, D. D. & Fleck, N. A. The Imperfection Sensitivity of Isotropic Two-Dimensional Elastic Lattices. *Journal of Applied Mechanics* **75**, 051011 (2008).

65. Meek, B., Van Der Auwear, H. & De Langhe, K. Challenges in NVH for Electric Vehicles. in *Proceedings of the FISITA 2012 World Automotive Congress* (eds. SAE-China & FISITA) vol. 191 675–685 (Springer Berlin Heidelberg, Berlin, Heidelberg, 2013).
66. Muhammad & Lim, C. W. Phononic metastructures with ultrawide low frequency three-dimensional bandgaps as broadband low frequency filter. *Sci Rep* **11**, 7137 (2021).
67. Meyer, P. P., Bonatti, C., Tancogne-Dejean, T. & Mohr, D. Graph-based metamaterials: Deep learning of structure-property relations. *Materials & Design* **223**, 111175 (2022).
68. Deng, B. *et al.* Inverse Design of Mechanical Metamaterials with Target Nonlinear Response via a Neural Accelerated Evolution Strategy. *Advanced Materials* **34**, 2206238 (2022).
69. Yang, R., Sun, X. & Narasimhan, K. A Generalized Algorithm for Multi-Objective Reinforcement Learning and Policy Adaptation. Preprint at https://doi.org/10.48550/ARXIV.1908.08342 (2019).
70. Buterez, D., Janet, J. P., Kiddle, S. J., Oglic, D. & Lió, P. Transfer learning with graph neural networks for improved molecular property prediction in the multi-fidelity setting. *Nat Commun* **15**, 1517 (2024).
71. Boley, J. W. *et al.* Shape-shifting structured lattices via multimaterial 4D printing. *Proc. Natl. Acad. Sci. U.S.A.* **116**, 20856–20862 (2019).
72. Dorléans, V., Delille, R., Notta-Cuvier, D., Lauro, F. & Michau, E. Time-temperature superposition in viscoelasticity and viscoplasticity for thermoplastics. *Polymer Testing* **101**, 107287 (2021).

Acknowledgments: We acknowledge Olivia Chen for her assistance in characterizing the commercial chest protector foams. We also thank Haotian Lu for his help in setting up the vibration experiments. We used OpenAI's ChatGPT (GPT-4) to assist in proofreading part of the abstract and main text of the manuscript, followed by human revision and editing.

Funding:

US National Science Foundation (NSF) DMREF grant 2119643
US National Science Foundation (NSF) grant 1829071
US National Science Foundation (NSF) grant 2106859
US National Science Foundation (NSF) grant 2312501
US Defense Advanced Research Projects Agency (DARPA) grant HR00112490370
US National Science Foundation (NSF) DMREF grant 2119545

Author contributions:

Conceptualization: XRZ, MM, WW, YS, MB, YJ,

Methodology: MM, DX, YTW, DY, XRZ, WW, YS, MB, YJ

Investigation: MM, DX, YTW, DY, DH, MO, AS

Visualization: MM, YTW, DY

Funding acquisition: XRZ, WW, YS, MB, YJ

Project administration: XRZ, MM, WW, YS, MB, YJ

Supervision: XRZ, WW, YS, MB, YJ

Writing – original draft: MM, DX

Writing – review & editing: MM, XRZ, DX, YTW, DY, MO, WW, YS, YJ

Competing interests: Authors declare that they have no competing interests.

A

Unit cell

Metamaterial-to-graph space

B

Nodes (V) Edges (E)

Graph: $G(V,E)$ ⟶ Topology

Node features

Coordinates x_i

Junction i

$v_i \in V$

Edge features

j

Strut r_{ij}

Length l_{ij}

i

$e_{ij} \in E$

Geometry

C

Graph generation

y

z

x

Cubic symmetry decomposition

Nodes

Edges

4

3

2

1

1 → 2 → 3 → 4

Topology generation

$\overline{\rho} \sim U([0.05, 0.25])$

Strut's radius, $r_{ij}(\overline{\rho}, \mathrm{L}, l_{ij})$

Relative density sampling

D

$\overline{\rho} = 0.0720$ $\overline{\rho} = 0.107$ $\overline{\rho} = 0.103$

$\overline{\rho} = 0.08$ $\overline{\rho} = 0.14$ $\overline{\rho} = 0.113$

$\overline{\rho} = 0.115$ $\overline{\rho} = 0.115$ $\overline{\rho} = 0.182$

E

Stress-strain

Upper bound σ_{UB}/E_s

Upper bound E_{UB}/E_s

Norm. stress σ/E_s (-)

$\sigma_{\max}/E_s \approx 5.4 \times 10^{-4}$

$\sigma_{\max}/E_s \approx 1.5 \times 10^{-3}$

$\sigma_{\max}/E_s \approx 3.6 \times 10^{-4}$

$\sigma_{\max}/E_s \approx 5.6 \times 10^{-4}$

$\sigma_{\max}/E_s \approx 1.2 \times 10^{-3}$

$\sigma_{\max}/E_s \approx 1.4 \times 10^{-4}$

$\sigma_{\max}/E_s \approx 4.9 \times 10^{-4}$

0

Strain, ε (%)

30

F

Vibration transmission

Upper bound T_{UB}

20

0

-120

Transmission, T (dB)

Lower bound T_{LB}

1

Frequency, f (kHz)

12

Fig. 1. Metamaterial-to-graph space and generation of diverse graph-response pairs. (**A**) Representative periodic truss metamaterial sampled from the test design space. The inset shows the corresponding unit cell. (**B**) Graph representation $G(V, E)$, with V a collection of nodes connected through edges E, of the metamaterial's unit cell in (**A**). Node v_i and edge e_{ij} features used to encode geometric information are shown as insets. Topological information is encoded as inductive bias into the graph connectivity by construction. (**C**) Generation of graphs with cubic symmetry to form our datasets. SRV graphs are generated by placing nodes along the edges of the SRV and connecting them to form a sequence, ensuring self-connectivity and cell-to-cell connectivity. Random node placement and sequence connection allow to create a large pool of diverse graphs. Relative density, $\overline{\rho}$ is randomly sampled from a uniform distribution $U(\overline{\rho})$, in the range $[0.05, 0.25]$. The strut radius, r_{ij} is accordingly obtained by $r_{ij}(\overline{\rho}, L, l_{ij}) = \sqrt{\overline{\rho}\frac{L^3}{\pi \sum_{i,j}^{N} l_{ij}}}$, where L is the unit cell size, l_{ij} is the strut length between node i and j, and N is the number of struts. (**D**) Examples of graphs in our datasets. A randomly sampled relative density is assigned to each randomly generated graph. (**E**) Stress-strain dimensionless curve space with seven highlighted representative examples extracted from the generated dataset (gray curves in background). The stress is normalized by the constitutive material's Young's modulus E_s. The curves are rescaled for illustration purposes. The normalized peak stress is thus reported on top of each curve. The stiffness and strength upper bounds, computed using the Voight bounds (rule of mixtures), delimit the design region of our framework. (**F**) Vibration transmission dimensionless curve space with six highlighted representative examples extracted from the generated dataset (gray curves in background).

A

GraphMetaMat

Policy network

Graph Encoder

Merger

Response Encoder

Action-u Decoder

u-th node embedding

Action-v Decoder

Action-stop Decoder

$\tilde{G}_k$

Decompose

G_k

Target curve

$\overline{y}$

u

v

G_{k+1}

Compose

$\tilde{G}_{k+1}$

Are the constraints satisfied?

Yes

$k = 1, \ldots, K$

Constraints

B

Self-connectivity

Face without nodes

Face with nodes

Cell-to-cell connectivity

$L_{\text{actual}} < L$

Face without nodes

$L_{\text{actual}} = L$

Face with nodes

Printability

Unsupported

Supported

C

Unsupported

Partially supported

$R_{\text{supp}} = 0.8$

Response

Target

Part. supp.

Self-supp.

Independent variable

Self-supported

$R_{\text{supp}} = 1$

Supported

D

Graph to CAD

CAD to 3D-printer

Response

Target

3D-printed

Independent variable

Fig. 2. Overview of GraphMetaMat. (**A**) Autoregressive policy network used to generate metamaterials (graphs) with target functional responses. At each step k, the SRV graph, G_k and the target curve, $\overline{y}$ are input into the model through a graph and response encoder, respectively. The policy network predicts the start node u and end node v to form a new edge, and the stop token S. When the generation stops (step K), the final SRV graph, G_K is transformed into the unit cell graph, $\tilde{G}_K$. During RL training, $\tilde{G}_K$ is input into the forward model to predict the functional response, guiding the policy optimization. (**B**) Three geometric and manufacturing constraints that can be enforced in GraphMetaMat. For each constraint, the top and bottom row show an example of missing and satisfied constraint, respectively. For instance, if the horizontal face of the SRV does not have any nodes, although the SRV graph is a connected sequence of nodes, self-connectivity is not satisfied. Additional constraints such as the maximum number of SRV graph nodes, $V_{\max}$ and the relative density, $\overline{\rho}$ bounds are constrained using GraphMetaMat. (**C**) Example of inverse designed unit cells with (right) and without (left) printability constraint, for a target stress-strain response curve. While achieving virtually identical response (FE-reconstructed curves in the plot), unlike the unconstrained design, the constrained structure is fully self-supported, i.e., it can be 3D-printed without adding external supports. R_{supp} is the degree of support, i.e., the fraction of supported nodes. (**D**) The generated unit cell graph is finally converted into a CAD model, tessellated periodically in space, 3D-printed using digital light stereolithography, and experimentally tested using universal testing machines or electrodynamical shakers along with laser vibrometers. The image shows a 3D-printed sample for target transmission response. Scale bar, 10 mm.

A

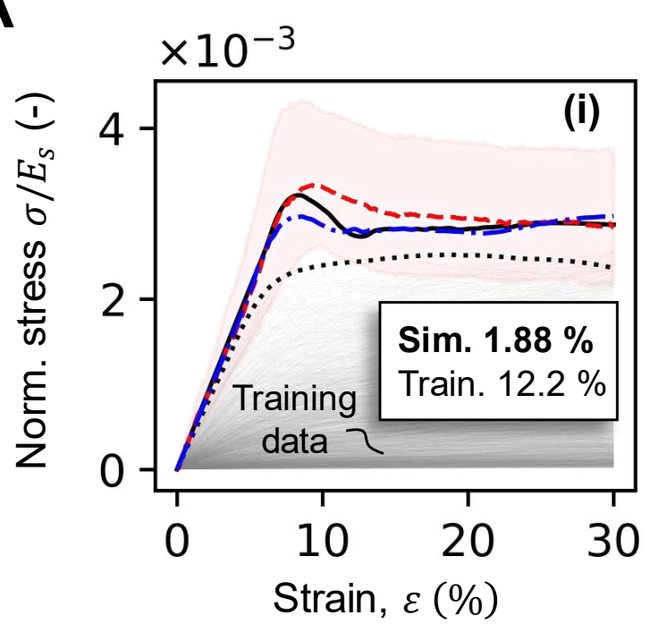

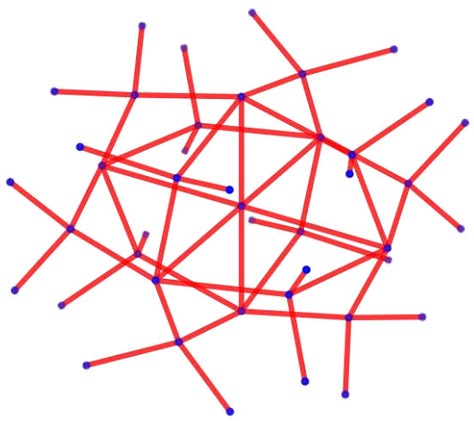

$\overline{\rho}$ = 20.3 %
($\overline{\rho}_{\text{train}}$ = 25 %)

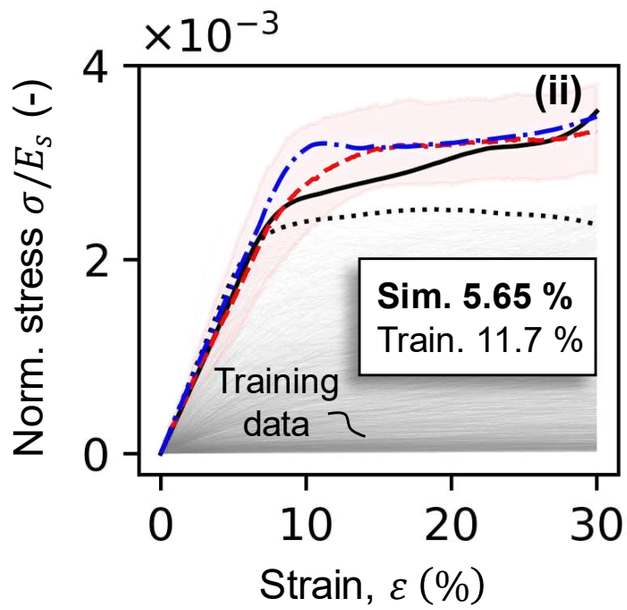

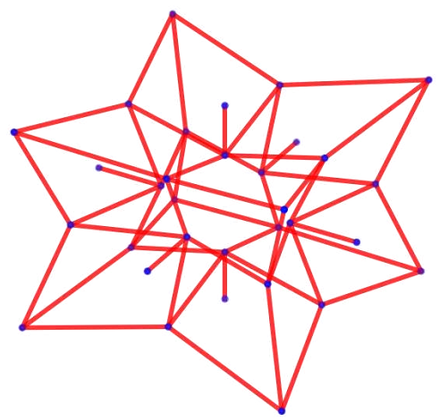

$\overline{\rho}$ = 21.4 %
($\overline{\rho}_{\text{train}}$ = 25 %)

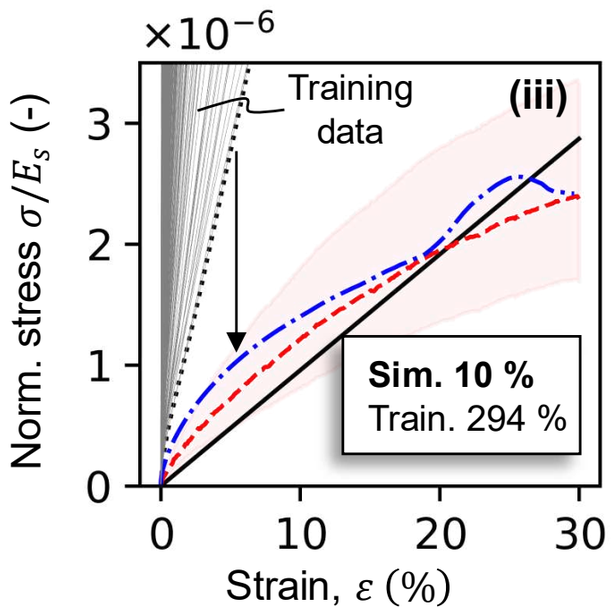

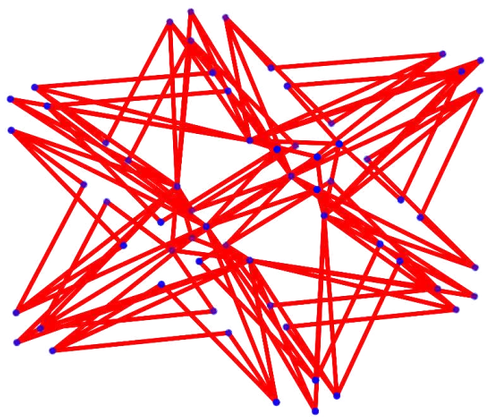

$\overline{\rho}$ = 2.0 %

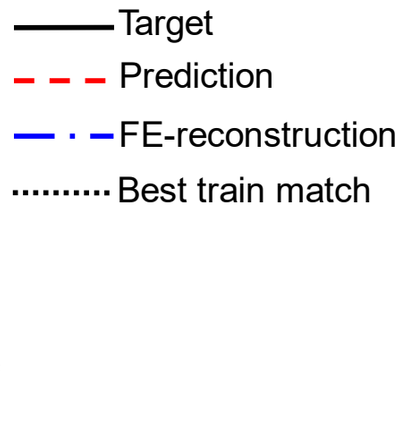

B

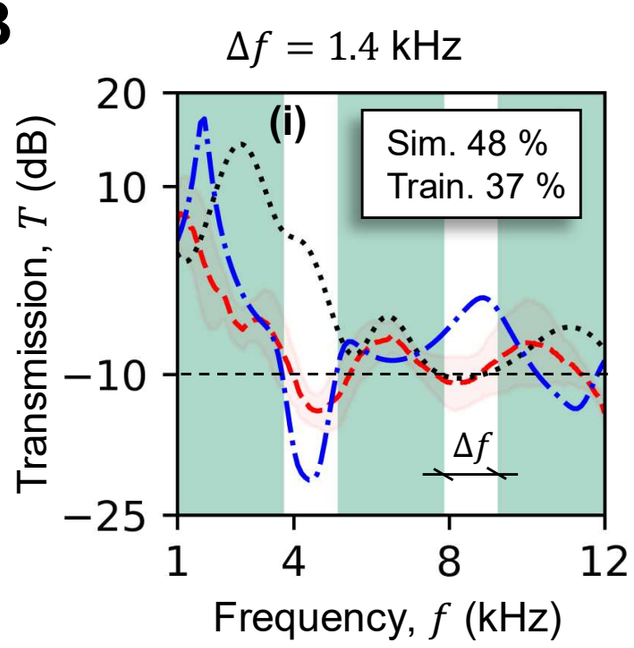

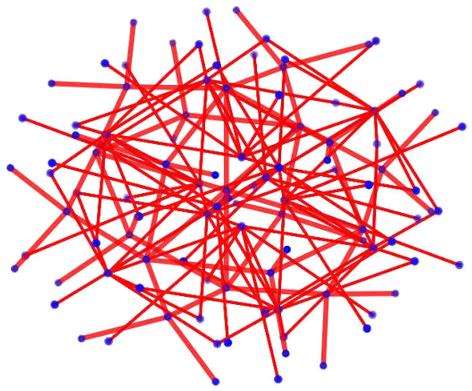

$\overline{\rho}$ = 11.5 %

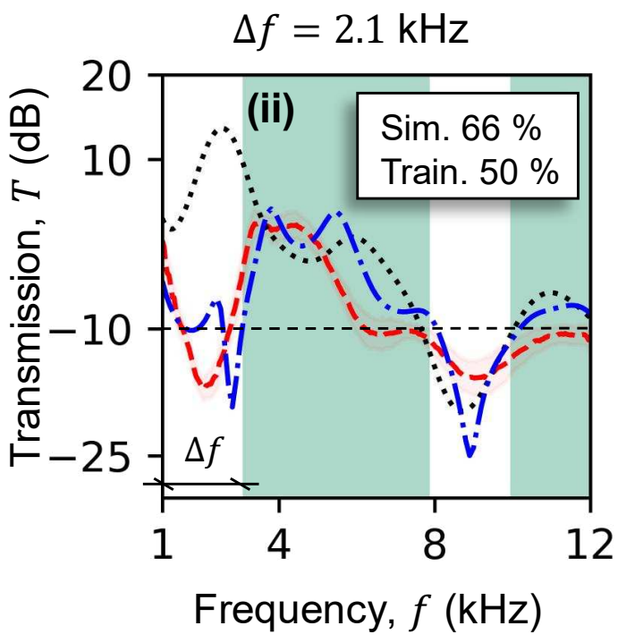

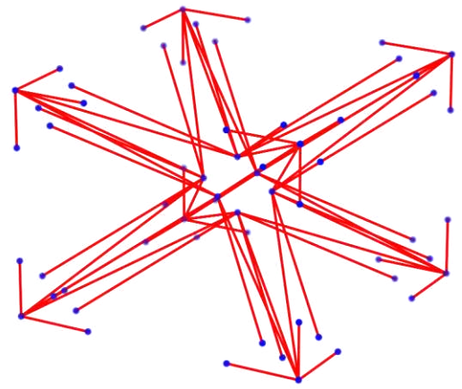

$\overline{\rho}$ = 12.1 %

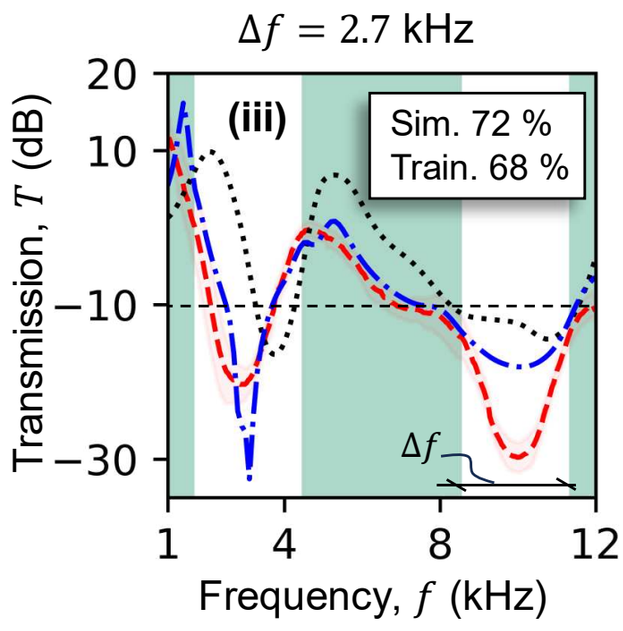

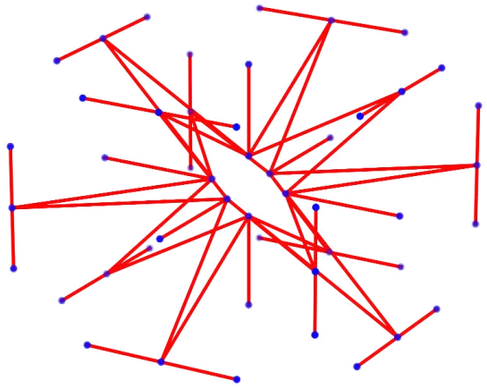

$\overline{\rho}$ = 10.5 %

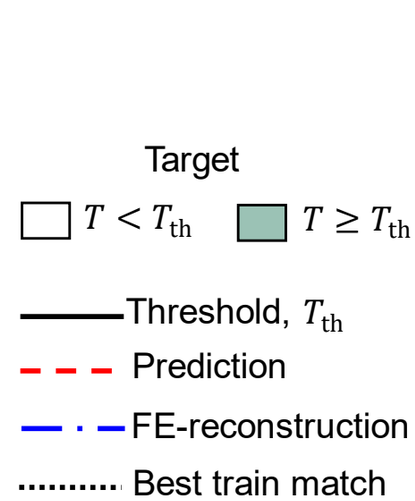

Fig. 3. Inverse design of representative user-defined nonlinear responses (unknown curve space). (**A**) Target stress-strain curves. (i), (ii), and (iii) correspond to strong elastic perfect-plastic, strong strain-hardening, and soft target responses, respectively. Strong curves exhibit a maximum stress higher than any training curve, while soft curves correspond to linear responses with stiffness significantly lower than that of the softest structure in the dataset. The boxes report the NMAE values between the target and FE-reconstructed curves ('Sim.'), and the target and best train match curves ('Train'). In all plots, stress is normalized by the constitutive material's Young's modulus E_s. (**B**) Target binary sequences. (i), (ii), and (iii) correspond to targets with two variable attenuation gaps of size $\Delta f = 1.4, 2.1, 2.7$ kHz, respectively. The boxes report the accuracy values between the target and FE-reconstructed curves ('Sim.'), and between the target and best train match curves ('Train'). For all accuracy calculations, the transmission threshold T_{th} is set to -10 dB.

A

Defects

Missing struts

Random

Delamination

Random

Broken struts

Localized

Non-uniformities

Radius variation

B

Graphs

Edge removal

z_d

Delamination plane

Intact struts

Removed struts

$\tilde{r}_{ij} = \alpha_{ij} r_{ij}$

r_{ij} → nominal radius

$\alpha_{ij} = 0$ for each $i - j$ missing strut

$\alpha_{ij} = 0$ for each $i - j$ broken strut

$\alpha_{ij} \sim \Gamma^{-1}(1, s)$ with $s > 0$, for each $i - j$ strut

C

Target response

Policy network

MCTS

Generated designs

$\bar{\rho}_1$ $\bar{\rho}_2$ $\bar{\rho}_3$ $\bar{\rho}_N$

Defect-aware message-passing

$\tilde{m}_{ij} = \boldsymbol{\alpha}_{ij}^4 \cdot m_{ij}(h_i, h_j, e_{ij})$

i j

h_{ij} → latent node

e_{ij} → edge feature

m_{ij} → message

$\boldsymbol{\alpha}_{ij}$ → **defects**

Graph Encoder

Magnitude Decoder

$\bar{\rho}$ Encoder

Shape Decoder

Forward model

D

Defect tolerance

Design with optimal defect tolerance

$\bar{\rho}$

Fig. 4. Defect-aware metamaterials design. (**A**) Three types of defects commonly found in additively manufactured metamaterials. (**B**) Graph representations of the defects shown in (A). (**C**) Inverse design workflow, incorporating the defect-aware message-passing physics-informed forward model. During inference, the message m_{ij} is modulated by a factor α_{ij}^4, depending on the defect type. For non-uniformities, α_{ij} is sampled from an inverse Gamma distribution (with unit mean and positive variance), commonly used for modeling positive-valued perturbations. The choice of exponent for α_{ij} follows from the mechanical assumption that strut stiffness scales with r_{ij}^4. The physics-informed component of the model is integrated into the Magnitude Decoder for stress-strain curve prediction, following $y = C\overline{\rho}^n$, where y represents the stress magnitude, and C and n are topology-dependent coefficients predicted by the decoder. (**D**) Defect tolerance is evaluated across generated designs, and the design with the highest robustness is selected.

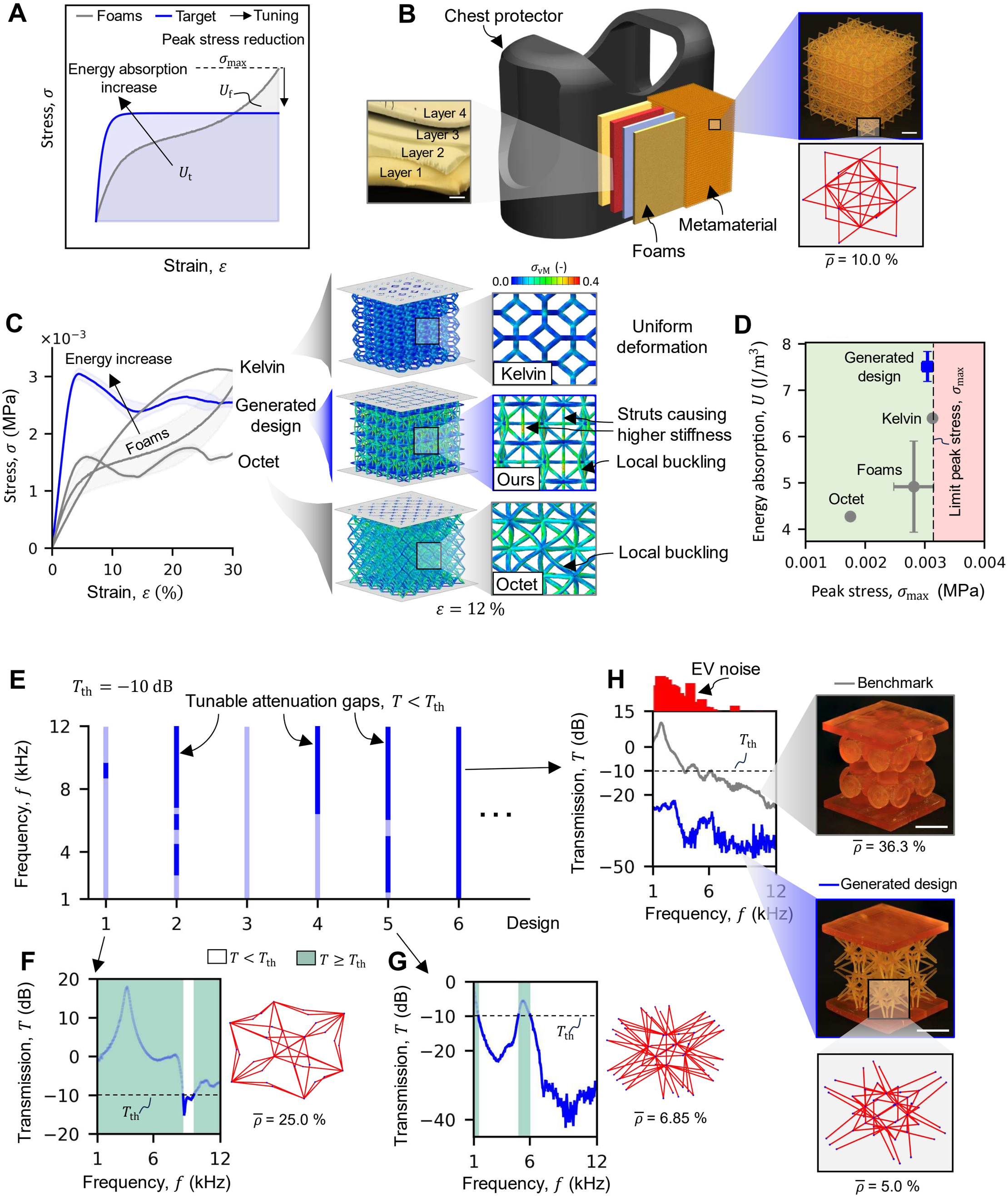
A
Foams
Target
Tuning
Peak stress reduction
Energy absorption increase
σ_{max}
U_f
U_t
Stress, σ
Strain, ε
B
Chest protector
Layer 4
Layer 3
Layer 2
Layer 1
Metamaterial
Foams
$\overline{\rho}$ = 10.0 %
C
$\times 10^{-3}$
Energy increase
Foams
Stress, σ (MPa)
Strain, ε (%)
Kelvin
Generated design
Octet
σ_{vM} (-)
0.0
0.4
Kelvin
Struts causing higher stiffness
Local buckling
Ours
Local buckling
Octet
Uniform deformation
ε = 12 %
D
Generated design
Kelvin
Foams
Octet
Limit peak stress, σ_{max}
Energy absorption, U (J/m^3)
Peak stress, σ_{max} (MPa)
E
T_{th} = −10 dB
Tunable attenuation gaps, $T < T_{th}$
Frequency, f (kHz)
Design
F
$T < T_{th}$
$T \geq T_{th}$
Transmission, T (dB)
Frequency, f (kHz)
$\overline{\rho}$ = 25.0 %
G
Transmission, T (dB)
Frequency, f (kHz)
$\overline{\rho}$ = 6.85 %
H
EV noise
Transmission, T (dB)
Frequency, f (kHz)
Benchmark
$\overline{\rho}$ = 36.3 %
Generated design
$\overline{\rho}$ = 5.0 %

Fig. 5. Metamaterial generation for impact protection and vibration attenuation. (**A**) Representative target stress-strain curve for cushioning application. The measured compressive response of stacked foam layers (identified as 'Foams') is used as baseline, with energy absorption, U_{f} and peak stress, $\sigma_{\max}^{\mathrm{f}}$. The target response is designed to have higher energy absorption, U_{t} and lower peak stress, $\sigma_{\max}^{\mathrm{t}}$, i.e., $U_{\mathrm{t}} \geq U_{\mathrm{f}}$ and $\sigma_{\max}^{\mathrm{t}} \leq \sigma_{\max}^{\mathrm{f}}$. The shaded areas identify the energy absorption, U. (**B**) Schematic model of a chest protector, highlighting foams from a commercial lacrosse chest protector and the GraphMetaMat-generated and 3D-printed design. Scale bars, 10 mm. (**C**) Experimental stress-strain curves of the generated design compared with those of the protector's foams ('Foams'), Kelvin foam, and octet structure. The generated design, Kelvin foam and octet structure were 3D-printed as $5 \times 5 \times 5$ periodic tessellated samples with same relative density $\overline{\rho} = 10\ \%$ (Methods). The shaded areas correspond to the measurement variability, obtained with at least three samples per structure. The insets next to the curves show the 3D view and 2D zoom-in of the corresponding FE deformed shapes and von Mises stress distribution at $\varepsilon = 12\ \%$, highlighting the deformation mechanisms of the considered metamaterials. (**D**) Summary plot of energy absorption, U vs. peak stress, $\sigma_{\max}$ for all experiments. The error bars correspond to the measurement variability across different samples. Error bars for octet and Kelvin foam are not visible due to lower variability. (**E**) Frequency vs. design plot, highlighting GraphMetaMat ability to design a large diversity of tunable attenuation gaps in the frequency range 1 – 12 kHz. (**F**) Generated unit cell graph along with the corresponding measured transmission response with small attenuation gap at higher frequencies. (**G**) Generated unit cell graph along with the corresponding measured transmission response with two large attenuation gaps at lower and higher frequencies. (**H**) Generated design with broadband attenuation gap in the whole frequency range, with potential applications to vibration-damping panels in EVs. The plot shows the average measured transmission responses of the corresponding 3D-printed $2 \times 2 \times 2$ samples of the generated design and the state-of-the-art locally resonant metamaterial[66]. Scale bar, 10 mm.

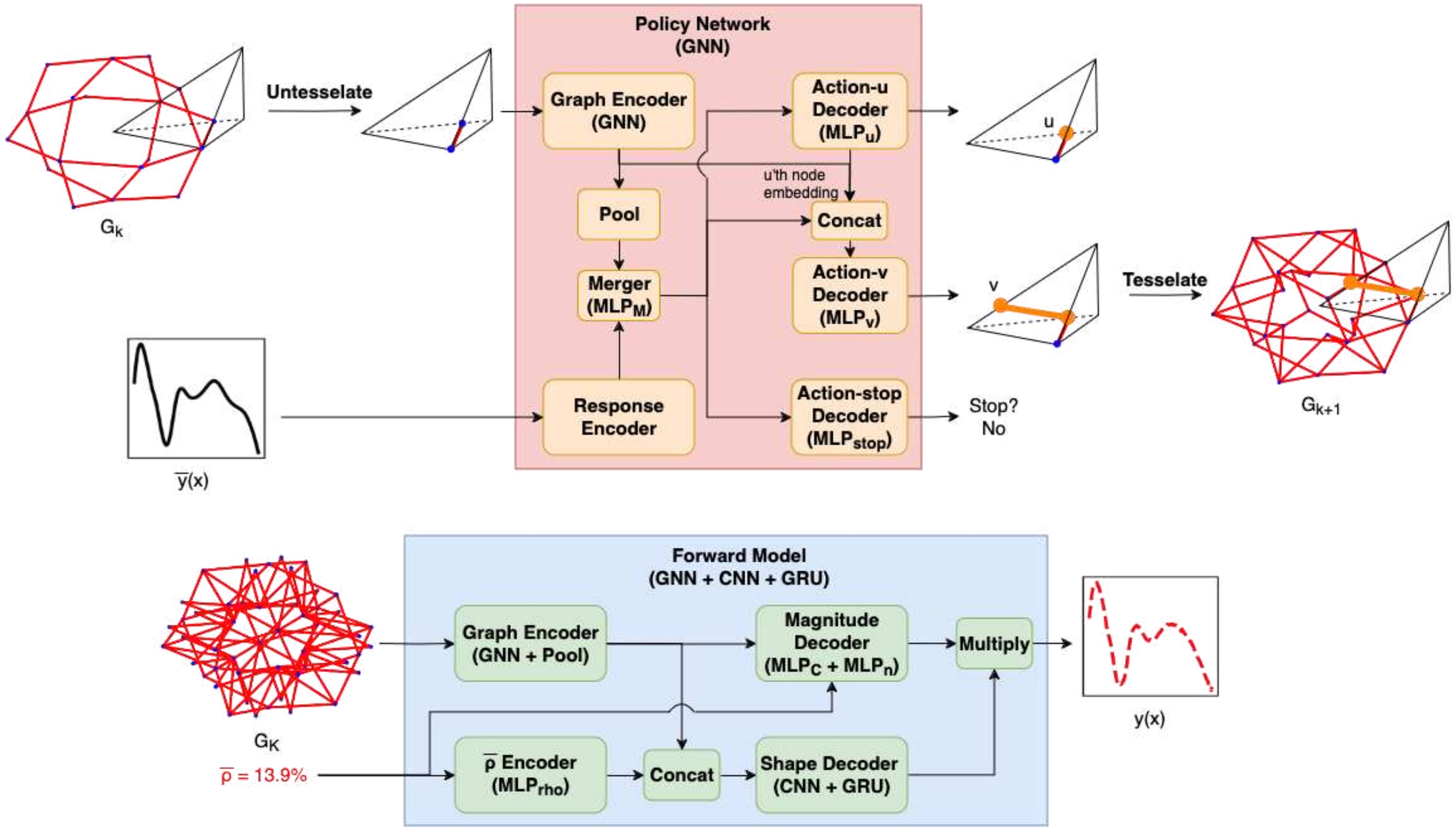

Extended Data Fig. 1. Schematic of the policy network (top) and forward model (bottom). The physics bias for stress predictions is encoded in the "Magnitude Decoder" of the forward model, predicting the coefficients C and n of the power-scaling law, $y_{max} = C\,\overline{\rho}^{n}$, with the relative density $\overline{\rho}$.

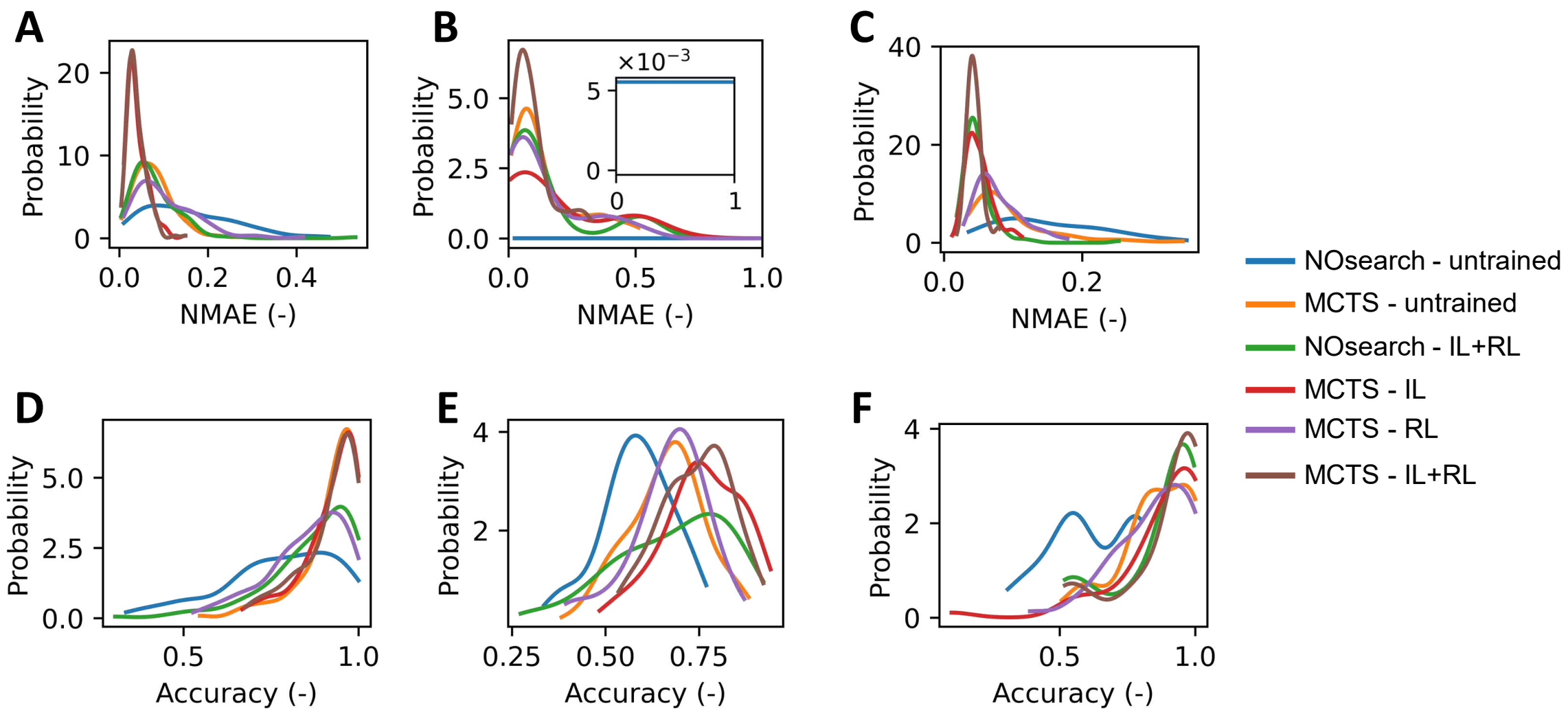

Extended Data Fig. 2. Ablation study to quantify the impact of search and policy training. Distribution of the relative error (NMAE) for stress-strain inverse design on the (**A**) 90:5:5 split test set, (**B**) user-defined target curves, and (**C**) energy absorbing-oriented target curves. Distribution of the accuracy for wave transmission inverse design on the (**D**) 90:5:5 split test set, (**E**) user-defined target sequences, and (**F**) noise control-oriented target responses. The relative error and accuracy are computed between the predicted responses of the generated metamaterials and the target responses. These results demonstrate how all components, from IL to RL and MCTS, contribute to the performance of our model.

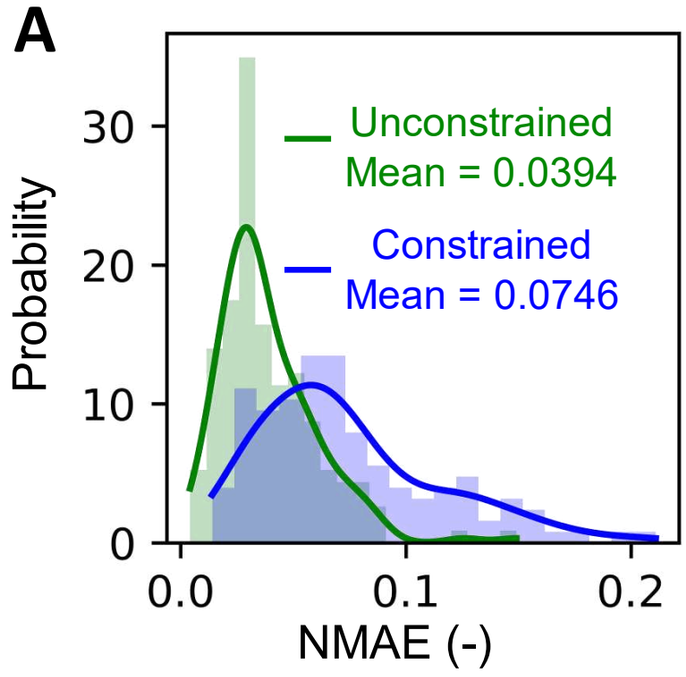
A
Probability
30
20
10
0
Unconstrained
Mean = 0.0394
Constrained
Mean = 0.0746
0.0
0.1
0.2
NMAE (-)

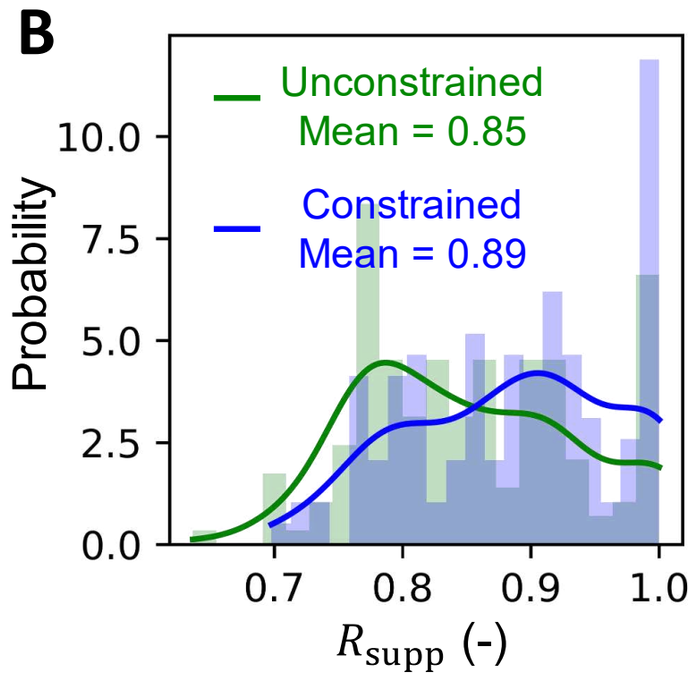
B
Probability
10.0
7.5
5.0
2.5
0.0
Unconstrained
Mean = 0.85
Constrained
Mean = 0.89
0.7
0.8
0.9
1.0
R_{supp} (-)

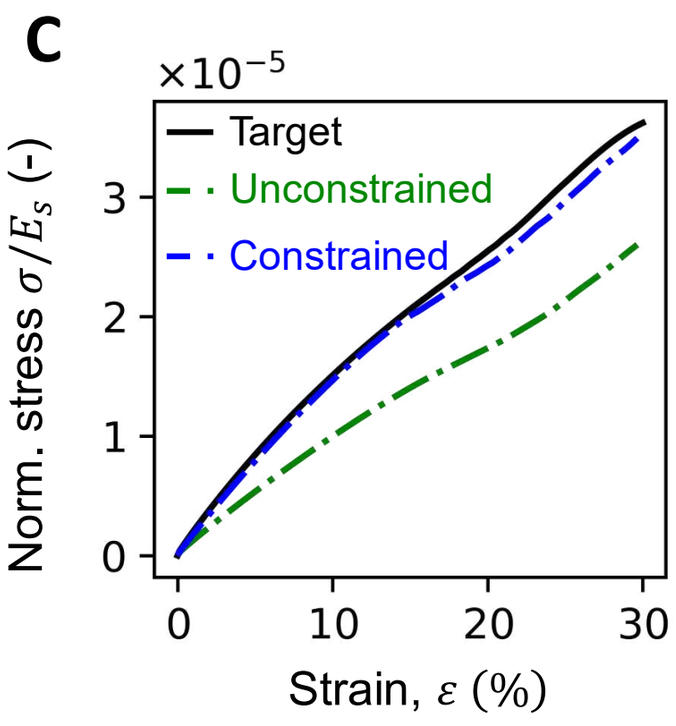
C
×10⁻⁵
Norm. stress σ/E_s (-)
Target
Unconstrained
Constrained
3
2
1
0
0
10
20
30
Strain, ε (%)

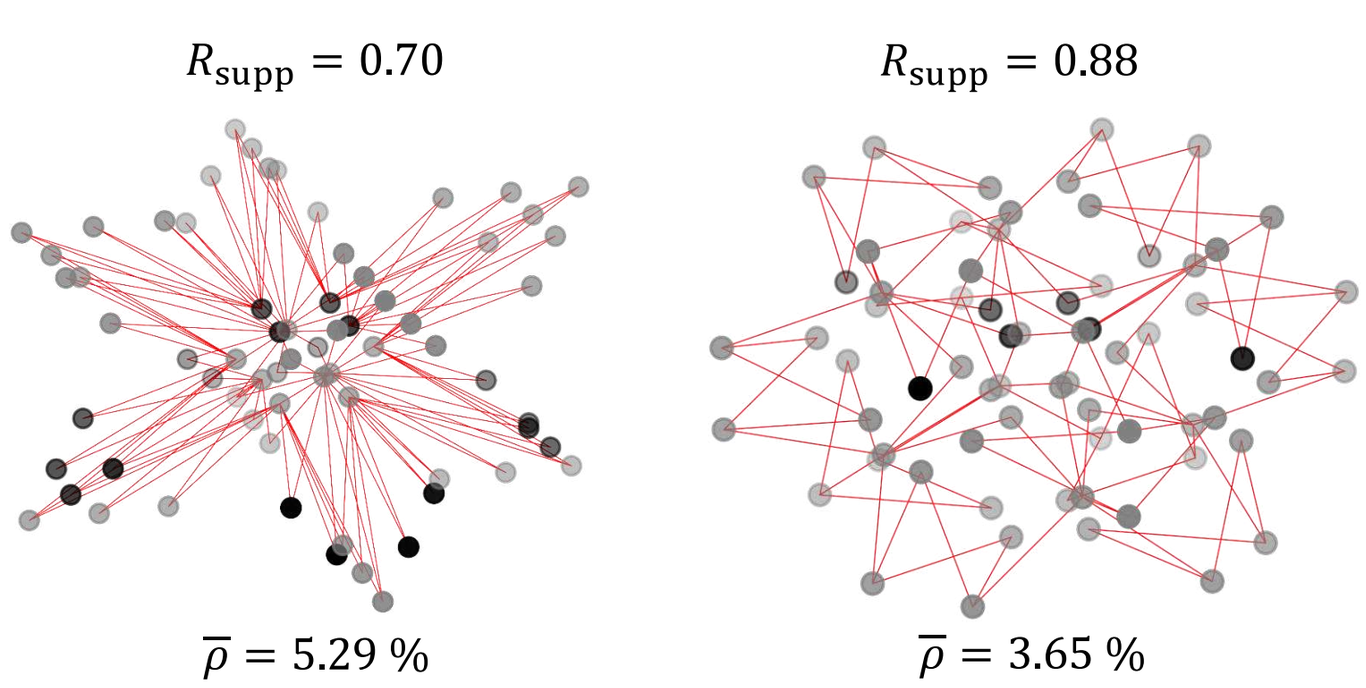
$R_{\mathrm{supp}} = 0.70$
$\overline{\rho} = 5.29$ %
$R_{\mathrm{supp}} = 0.88$
$\overline{\rho} = 3.65$ %
Unsupported
Supported

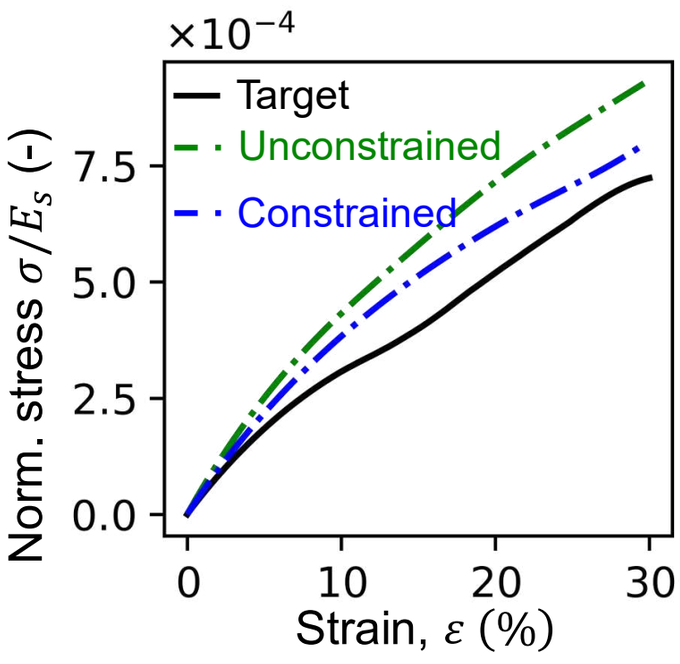
×10⁻⁴
Norm. stress σ/E_s (-)
Target
Unconstrained
Constrained
7.5
5.0
2.5
0.0
0
10
20
30
Strain, ε (%)

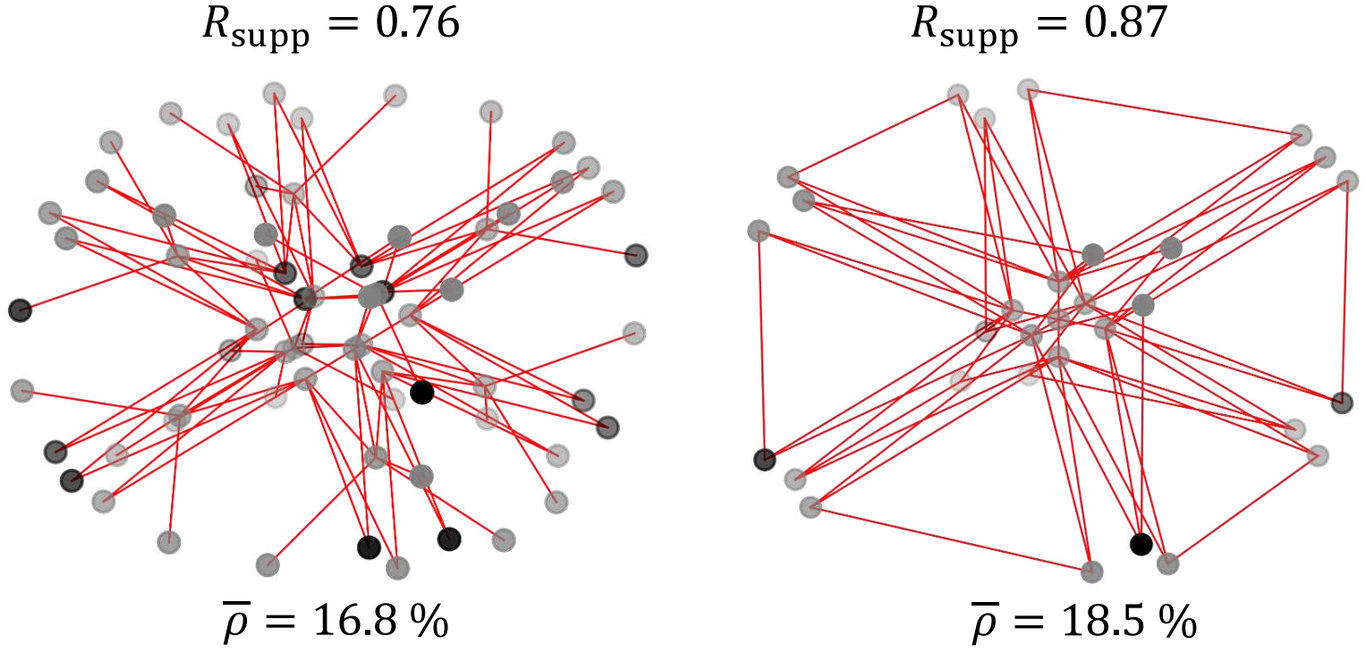
$R_{\mathrm{supp}} = 0.76$
$\overline{\rho} = 16.8$ %
$R_{\mathrm{supp}} = 0.87$
$\overline{\rho} = 18.5$ %

843

Extended Data Fig. 3. Impact of printability constraint. (**A**) Distribution of the relative error (NMAE) between the target and predicted test stress-strain responses, with and without printability constraint. (**B**) Distribution of the degree of support, R_{supp} of the generated graphs on the test stress-strain target responses, with and without printability constraint. (**C**) Two examples of generated structures with and without printability constraint along with the corresponding FE-reconstructed stress-strain curves. These results reveal that, for certain target responses, printable structures can outperform non-printable truss networks. Overall, GraphMetaMat demonstrates the new capability of encoding manufacturing constraints, and offers flexibility in balancing performance and manufacturability constraints, as highlighted in (A) and (B).

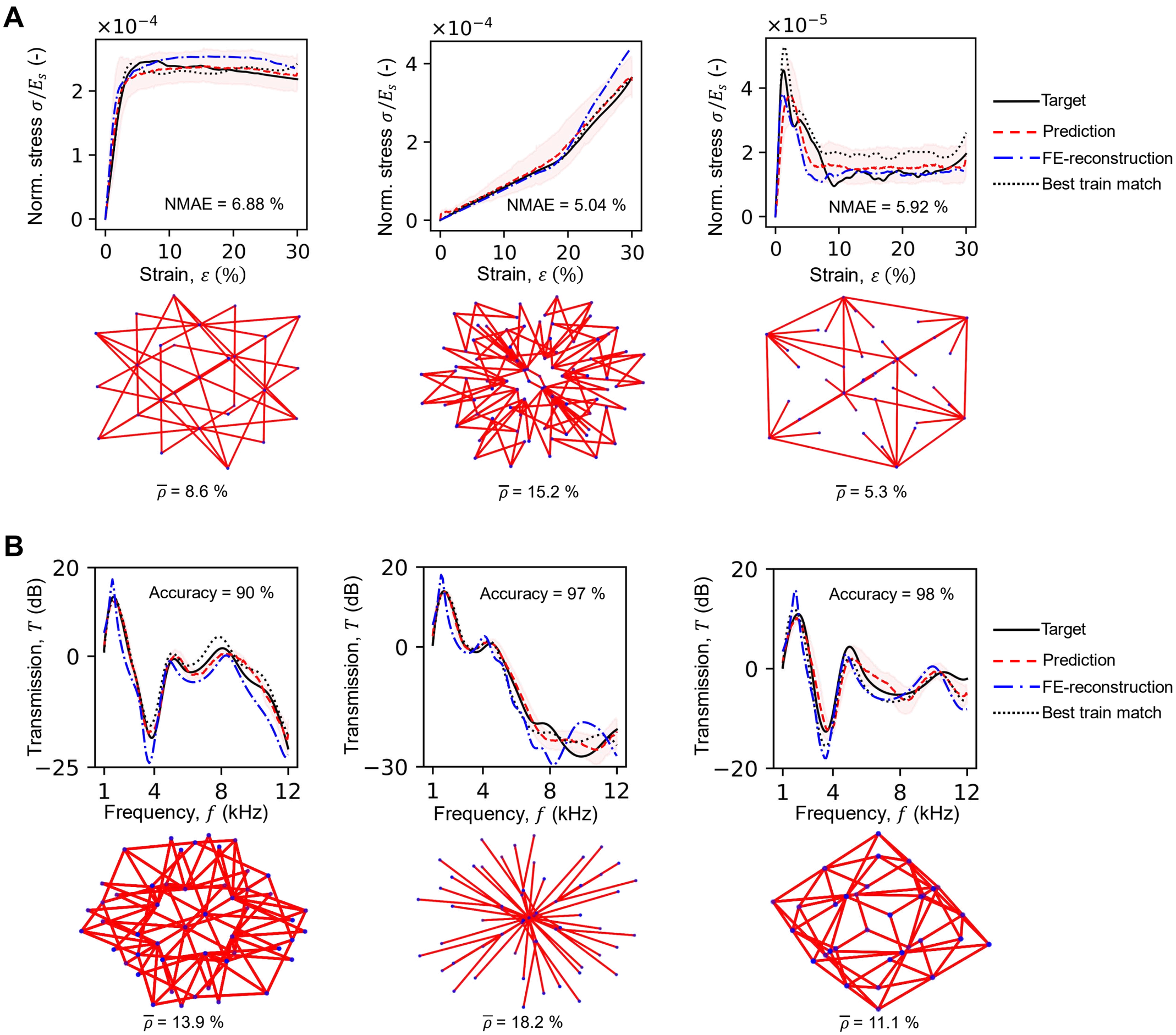

Extended Data Fig. 4. Inverse design of representative unseen nonlinear responses (known curve space). (**A**) Target stress-strain curves from the test set. NMAE values are computed between the target and FE-reconstructed curves. Stress is normalized by the constitutive material's Young's modulus E_s. (**B**) Target transmission curves from the test set. Accuracy values are computed between the target and FE-reconstructed curves using a transmission threshold of $T_{th} = -10$ dB.

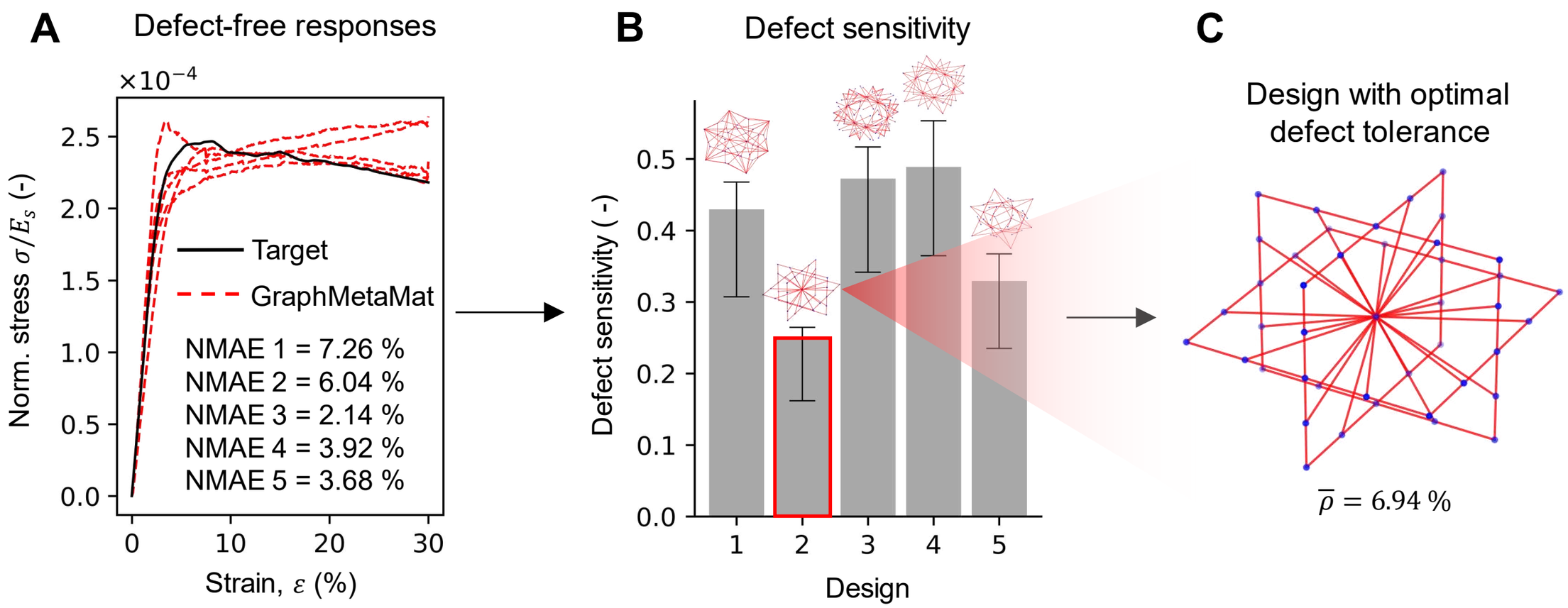

857

858 **Extended Data Fig. 5. Example of defect-aware inverse design.** (**A**) Target and predicted defect-free stress-strain curves of five generated designs.
859 (**B**) Defect sensitivity of the five designs, defined as $1 - \overline{J}$, where $\overline{J}$ represents the average curve similarity between pristine and flawed design
860 responses across different defect parameters, such as the fraction of broken struts. Error bars indicate the forward model's estimated uncertainty.
861 (**C**) Design 2 identified as the metamaterial with optimal defect tolerance.

	GraphMeta Mat	VAE	Tandem	Diffusion	GAN
3D – truss	✓	✓	✓	✗	✗
Large design space	✓	✓	✗	✓	✓
Nonlinear responses	✓	✓	✓	✓	✓
Large response variability	✓	✗	✗	✗	✗
Low-data regimes	✓	✗	✓	✗	✗
Topology and size independent	✓	✗	✗	✗	✗
Extrapolation capabilities	✓	✓	✗	✓	✗
Geometric constraints	✓	✗	✗	✗	✗
Defect-aware design	✓	✗	✗	✗	✗

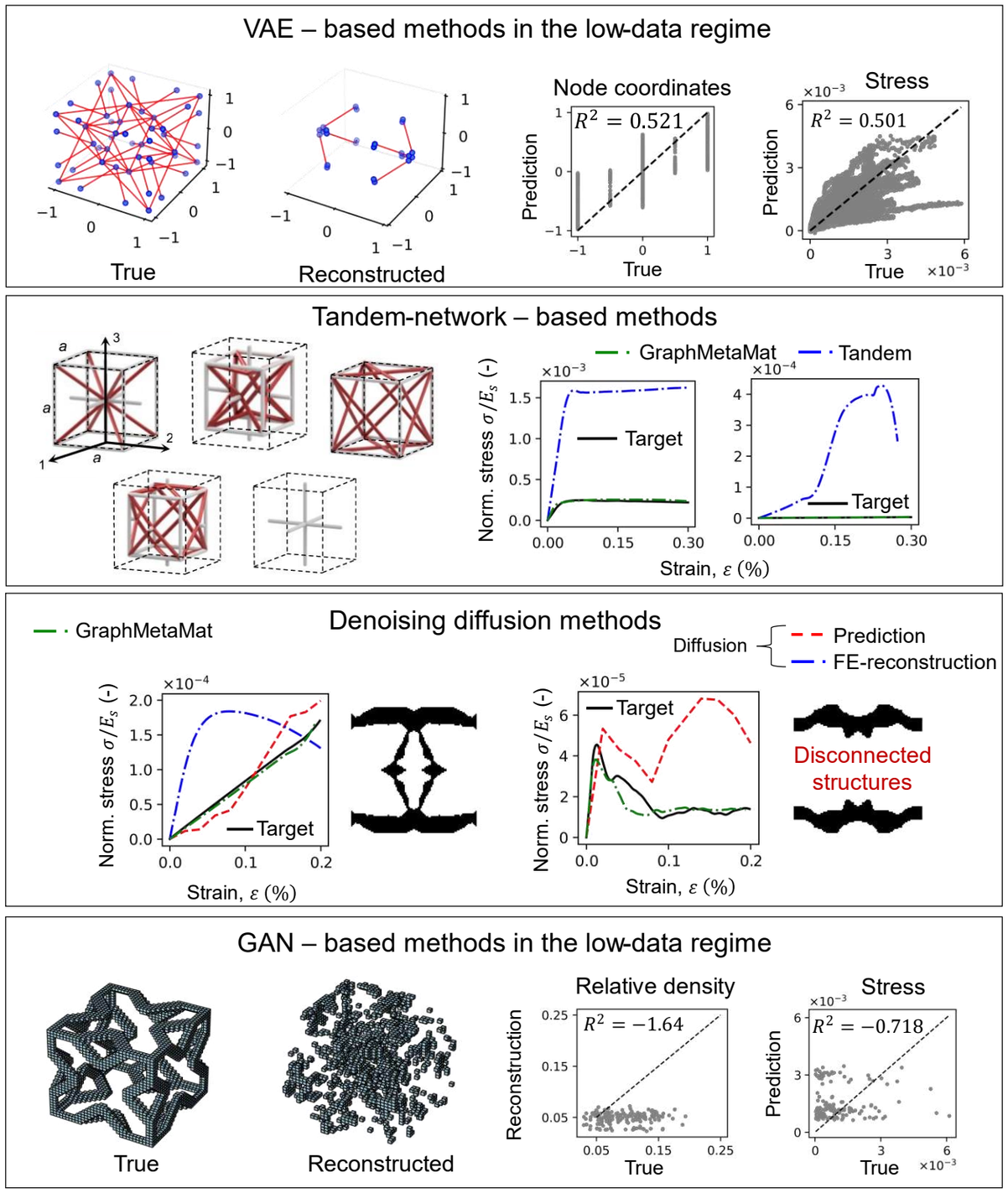

Extended Data Fig. 6. Benchmark summary between GraphMetaMat and state-of-the-art inverse-design methods. VAE-based method refers to ref.[51]. Tandem-network method refers to ref.[50]. Denoising diffusion method refers to ref.[28]. GAN-based method refers to ref.[45].

Extended Data Table 1. Performance comparison between GraphMetaMat and prior generative methods: VAE-based approach (ref.[51]), tandem network (ref.[50]), denoising diffusion model (ref.[28]), and conditional GAN (ref.[45]). Stress-strain responses from the test set (90/5/5 train/validation/test split) are used as targets. Reported values are the normalized mean absolute errors (NMAE) between the target and FE-reconstructed curves and the fraction of self-connected and periodic compatible (valid) structures. The VAE and GAN models were trained on our dataset. The tandem network was trained on the dataset from ref.[50] due to its fixed topology representation. The diffusion model was trained on the 2D pixel-based dataset from ref.[28] as it cannot represent 3D truss metamaterials. For GraphMetaMat, we report two NMAE values: one for stress-strain curves up to 30% strain, and one up to 20% to enable direct comparison with the diffusion model, which is limited to that strain range.

	GraphMetaMat	VAE	Tandem network	Diffusion	GAN
Target vs. FE-reconstructed curve	**10.4 – 13.6 %**	No valid structures	> 100 %	35 %	No valid structures
Fraction of valid structures	**100 %**	No valid structures	100 %	74 %	No valid structures